nature geoscience

SUPPLEMENTARY INFORMATION

DOI: 10.1038/NGEO2912

In the format provided by the authors and unedited.

Smaller desert dust cooling effect estimated from analysis of dust size and abundance

Jasper F. Kok[1,*], David A. Ridley[2], Qing Zhou[3], Ron L. Miller[4], Chun Zhao[5], Colette L. Heald[2,6], Daniel S. Ward[7], Samuel Albani[8], and Karsten Haustein[9]

[1]Department of Atmospheric and Oceanic Sciences, University of California, Los Angeles, CA 90095
[2]Department of Civil and Environmental Engineering, Massachusetts Institute of Technology, Cambridge, Massachusetts, United States
[3]Department of Statistics, University of California, Los Angeles, CA 90095
[4]NASA Goddard Institute for Space Studies, New York NY 10025
[5]School of Earth and Space Sciences, University of Science and Technology of China, Hefei, Anhui, China
[6]Department of Earth, Atmospheric and Planetary Sciences, Massachusetts Institute of Technology, Cambridge, MA, USA
[7]Program in Atmospheric and Oceanic Sciences, Princeton University, Princeton, NJ, USA
[8]Laboratoire des Sciences du Climat et de l'Environnement, CEA-CNRS-UVSQ, Gif-sur-Yvette, France
[9]School of Geography and the Environment, University of Oxford, Oxford OX1 3QY, UK
[*]e-mail: jfkok@ucla.edu

Supplementary Figures

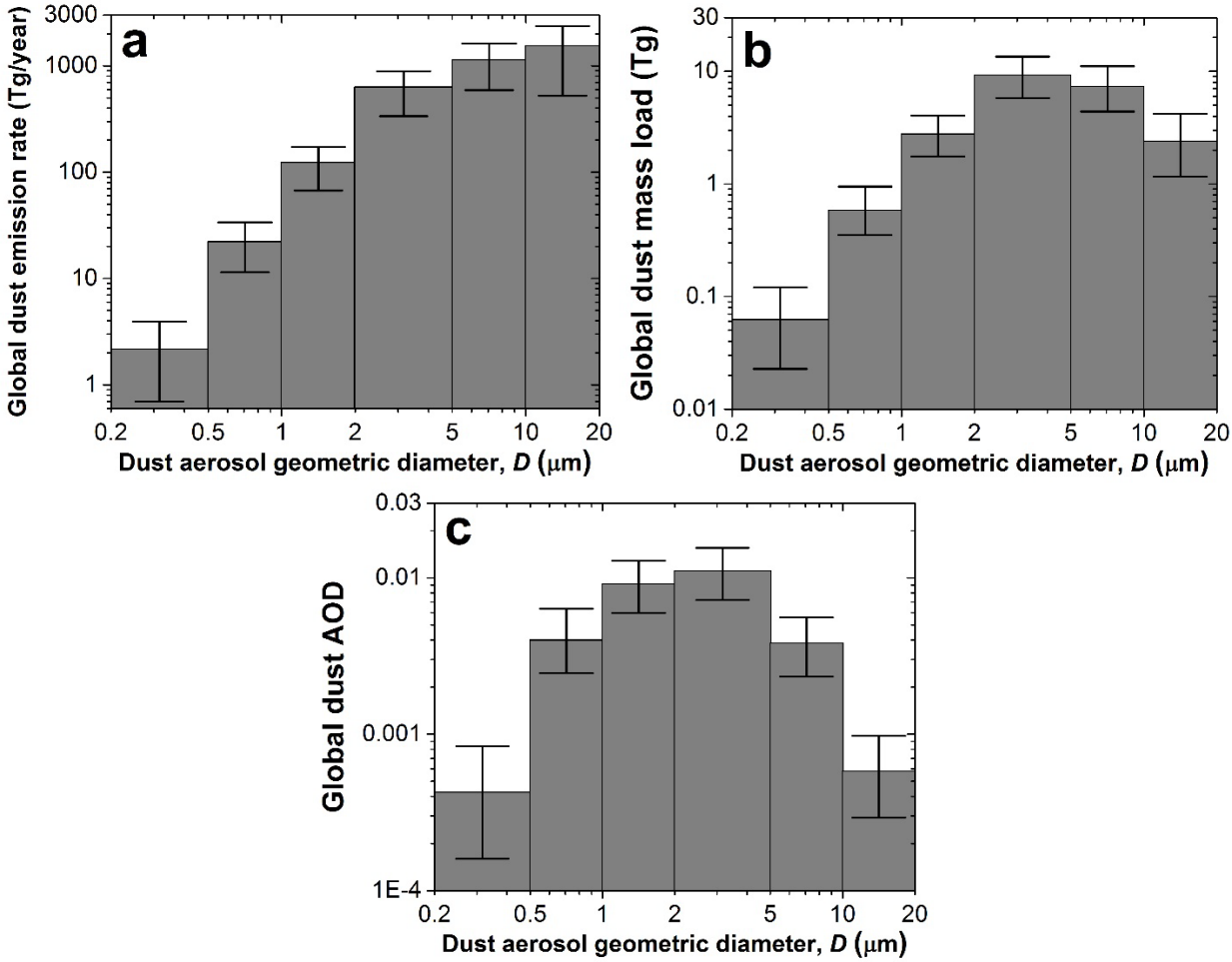

Supplementary Figure S1. Contributions of individual particle size ranges to the global dust budget. Size-resolved contributions to (**a**) the global dust emission rate, (**b**) global dust mass loading, and (**c**) global DAOD. Results are obtained by integrating the constraints on size-resolved dust emission, loading, and DAOD (see Fig. 2 and Section 3) between the bin size limits. Clay-sized aerosols ($D \leq 2$ μm) make up a small fraction of the emitted dust, but an increasingly large fraction of the mass load and global DAOD. Conversely, very coarse dust ($D \geq 5$ μm) accounts for the majority of the emitted dust, but much smaller fractions of the mass load and global DAOD. Error bars denote each particle bin's CI.

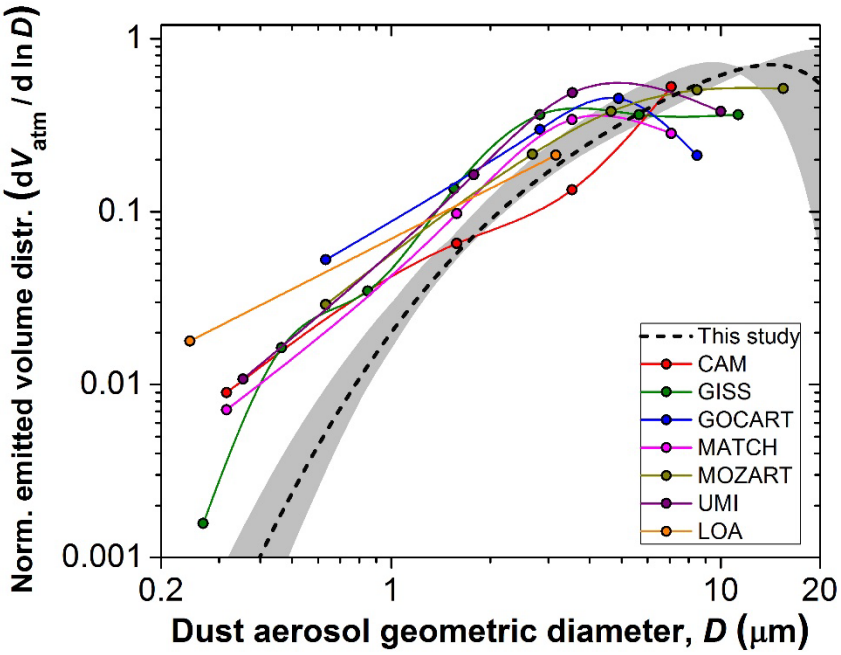

Supplementary Figure S2. Normalized size distribution of emitted dust. The normalized size distribution of dust at emission, as constrained here based on measurements (dashed line with shading for CI; from Fig. 1c), and as assumed in seven AeroCom models (colored lines). Models overestimate the contribution of clay-sized aerosols and underestimate the contribution of very coarse (D ≥ 5 μm) aerosols. Both the experimentally-constrained and modeled size distributions were normalized to unity over the PM_{20} size range (see Materials and Methods).

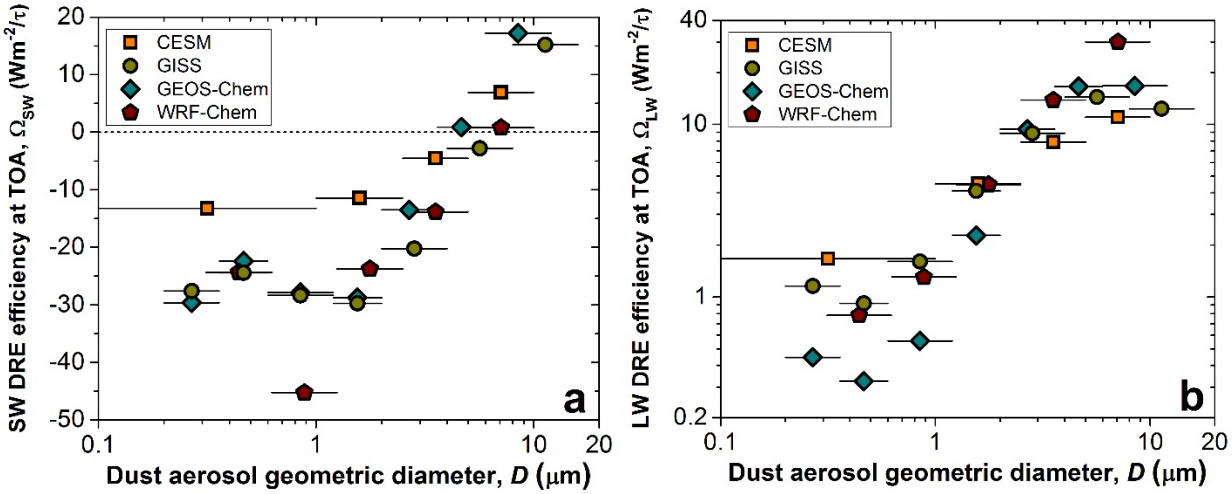

Supplementary Figure S3. The size-resolved direct radiative effect efficiency. Results for the direct radiative effect efficiency, which is the DRE produced per unit global DAOD, are shown for individual particle bins simulated by four different global models in both the SW (**a**) and LW (**b**) spectra. The LW radiative effect efficiency includes the effects of LW absorption only; the effect of LW scattering is not included in most global models[1, 2]. The horizontal black lines denote the particle bin's size limits.

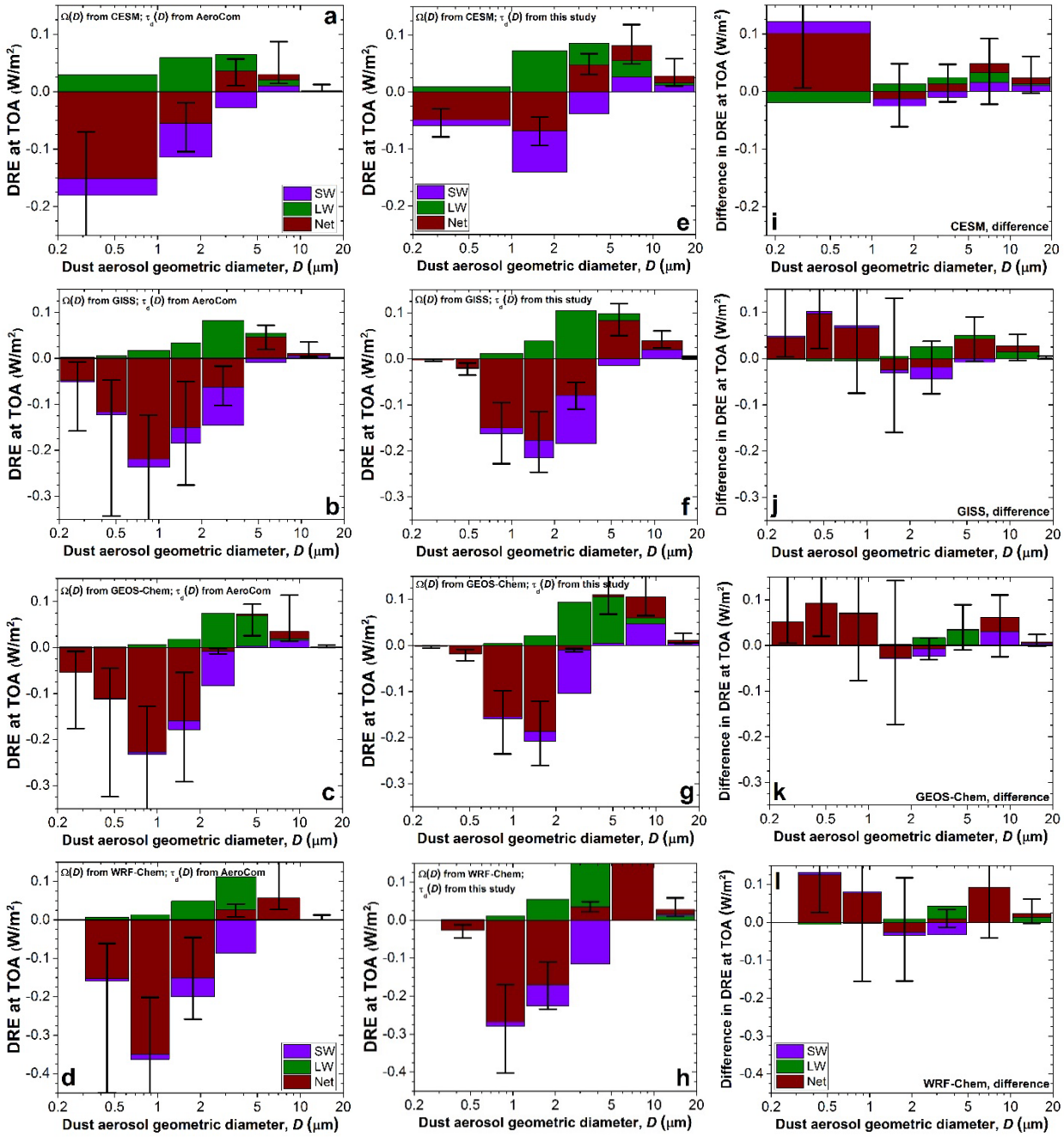

Supplementary Figure S4. The size-resolved direct radiative effect (DRE) at top-of-atmosphere (TOA). Panels (**a**-**h**) show the DRE calculated for each particle bin of the four global models CESM, GISS, GEOS-Chem and WRF-Chem. All results were obtained by multiplying the DAOD for each particle bin [$\Delta\tau_d$; Eq. (S.29)] by the corresponding model's radiative effect efficiency [$\Omega(D)$; Fig. S3]; see Section 4 for details. Results in panels (**a**-**d**) used the size-resolved DAOD obtained by combining the size-resolved dust loading from the seven AeroCom models with Mie theory for each particle bin (see Section 4.1), whereas panels (**e**-**h**) used the constraints on the size-resolved DAOD from this study (see Section 4.2). Panels (**i**-**l**) show the difference between the two treatments. Results are shown for DRE due to dust interactions with SW (purple bars), LW (green bars), and all radiation (brown bars). To prevent cluttering the graphs, only the uncertainty in the DRE due to interactions with all radiation is shown. For all four models, correcting the fine size bias of the AeroCom models decreases the cooling by submicron dust (D < ~1 μm), and increases the warming by coarse dust (D > ~5 μm).

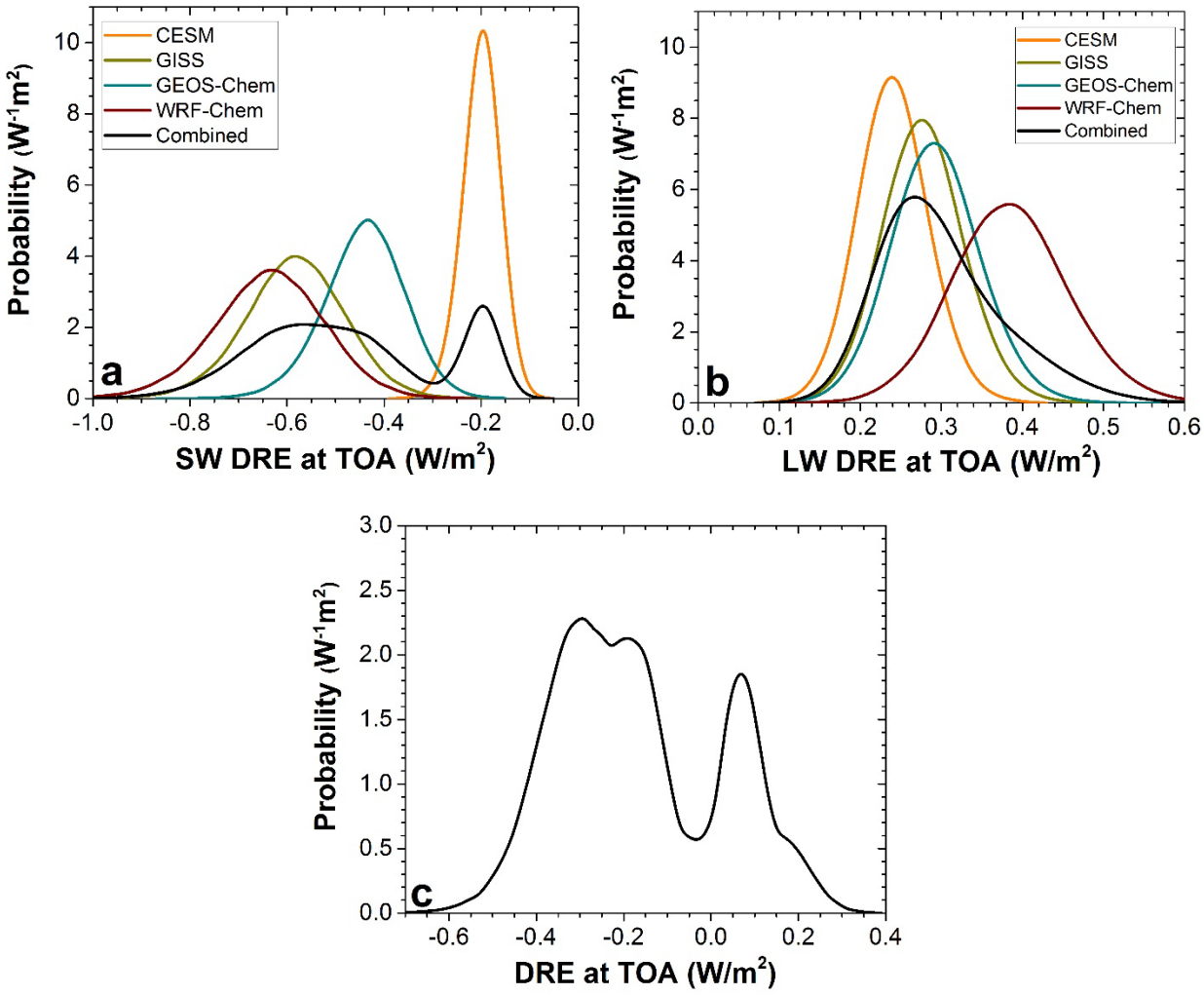

Supplementary Figure S5. Probability distributions of the dust direct radiative effect (DRE). The probability distribution of the DRE in the SW (**a**) and LW (**b**) spectra are shown for each of the three global models, as well as the resulting probability distribution of the total DRE (**c**). These probability distributions are obtained by combining constraints on the size-resolved global dust optical depth (Fig. 2c) with global model calculations of the DRE per unit optical depth in the SW and LW spectra (Fig. S3).

Supplementary Methods

This section first provides a detailed description of our methodology for obtaining the globally-averaged atmospheric dust size distribution (Section 1), the extinction efficiency (Section 2), the size-resolved global dust emission rate, loading, and optical depth (Section 3), and the dust direct radiative effect (Section 4). We then provide a description of the atmospheric model simulations used in this study (Section 5).

1. Analysis of the globally-averaged atmospheric dust size distribution

Using Equation (3) in the main text, we obtain the globally-averaged particle size distribution (PSD) of atmospheric dust from constraints on the emitted dust PSD (Section 1.1) and the size-resolved dust lifetime (Section 1.2). The resulting globally-averaged atmospheric dust PSD (see Section 1.3) is compared against that obtained by a number of global model simulations (see Section 1.4).

1.1 Globally-averaged dust PSD at emission

The size distribution of dust at emission has been measured by a total of seven studies[3-9]. These studies measured the emitted dust number size distribution, using optical microscopy of collected dust samples[3-5], or optical particle counters used on the ground[6-8] or on an airplane flying in the boundary layer[9]. Below, we describe the procedure for analyzing these measurements, and also provide a description of each study and the methods employed by it. We then describe the procedure for constraining the globally-averaged emitted dust size distribution in Section 1.1.2.

1.1.1 Analysis of the emitted dust PSD data sets

In order to use the seven studies of the emitted dust PSD to constrain the globally-averaged emitted dust PSD, we first need to bring the different data sets on an equal footing. The procedure for this largely follows that described in Ref. [10], with exceptions for each data set described below. Specifically, because emitted dust size distribution measurements are generally well-described by the power law $dN_{\text{emit}} / d\ln D \propto D^{-2}$ in the range of 2 – 10 μm (see Fig. 2 in Ref. [10]), we fit each set of measurements in that size range for a given wind speed and soil (or location) to this power law. We then normalized measurements at all aerosol sizes for a given soil and wind speed by the proportionality constant in the fitted power law to account for the strong dependence of the dust flux on wind speed and soil type[11-13]. For a given study, this procedure put measurements at different wind speeds and for different soils on an equal footing, except for the dependence of the shape of the dust PSD on wind speed and soil properties, which measurements suggest is small[14].

For each data set, we reduced random errors by averaging over all normalized measurements for a given particle bin for different wind speeds, soils (in the case of Ref. [5]), and terrain types (in the case of Ref. [9]). This procedure also yielded the standard error of measurements for a given particle bin, which thus does not include any systematic errors inherent in the measurement technique. Since Ref. [3] obtained only one reliable measurement per particle size, the standard error on these single measurements was estimated from the similar measurements of Ref. [4] and [5]. The result of the above procedure is plotted in Figure 1c.

We note that the random error obtained through the above procedure is small compared to the spread between measurements from different studies (see, e.g., fig. 5 in Ref. [9] and fig. 3 in Ref. [15]). We thus infer that random errors within a data set, which capture measurement uncertainty and the effects of differences in wind speed and soil/terrain type (for Refs. [5] and [9]), are small compared to the systematic errors between data sets. This inference is supported by the fact that measurements from different soils within a given study are very small [see Fig. 2 in Ref. [10] and Fig. 5 in Ref. [9]], and that changes in wind speed have been shown to have no statistically significant influence on the size distribution of emitted PM_{10} dust[14]. This important observation implies that differences in measurements of the emitted dust size distribution are largely due to differences in the measurement technique rather than to differences in the actual size distribution of emitted dust aerosols. Further, since the difference in the emitted dust PSD for different soils, terrain types, and wind speeds is small compared to the systematic error between data sets, we can

consider each data set as an approximate measure of the globally-averaged emitted dust size distribution (also see discussions in Refs. [10], [14], and [16]). This is consistent with the finding that in situ dust size distributions appear independent of source region[16, 17].

1.1.1.1 Gillette data set

The first field measurements of the size-resolved vertical dust flux were made by Gillette and co-workers[3-5]. They reported measurements of one sandy loam, two fine sand, and two loamy fine sand soils in Texas and Nebraska for a range of wind (friction) speeds. These measurements were made using two single-stage jet impactors at heights of 1.5 and 6 m. The collected aerosols were subsequently analyzed using optical microscopy to retrieve the size-resolved vertical flux of dust aerosols larger than ~1 μm geometric diameter. Because systematic errors due to differences in measurement technique between data sets are much greater than the random errors due to differences in soil and wind speed within a given data set, we combine the results from the three Gillette studies[3-5] into a single data set.

1.1.1.2 Fratini et al. (2009) data set

Fratini et al.[6] used eddy covariance to measure the size-resolved flux of dust emitted over a sandy soil in the Gobi desert in Inner Mongolia, China. The dust particle concentration was measured using an optical particle counter (OPC), which measured particles with aerodynamic diameters between 0.35 and 9.5 μm. These measurements thus need to be corrected to the geometric size range. The geometric and aerodynamic diameters are related by[18, 19]

$$D_{\mathrm{d}} = \sqrt{\frac{\chi \rho_0}{\rho_{\mathrm{p}}}} D_{\mathrm{ae}}, \tag{S.1}$$

where $\rho_{\mathrm{p}} \approx 2.5 \pm 0.2 \times 10^3$ kg/m^3 is the density of dust aerosols (see main text), and χ is the dynamic shape factor, which is defined as the ratio of the drag force experienced by the irregular particle to the drag force experienced by a spherical particle with diameter D_{d} [18]. Measurements of the dynamic shape factor for mineral dust particles with a geometric diameter of ~10 μm find $\chi \approx 1.4 \pm 0.1$ [20-22]. Inserting this into equation (S.1) then yields that $D_{\mathrm{d}} \approx (0.75 \pm 0.04)\, D_{\mathrm{ae}}$, where the standard error was obtained using error propagation[23]. Note that the Fratini et al. results from the coarser particle bins ($> \sim 5$ μm) are unreliable because the efficiency of the air inlet system was not tested and could have produced an under-sampling of larger particles (Fratini, 2012, personal communication). Consequently, we did not use these measurements, and normalized the Fratini et al. data over the range of 2–4 μm (instead of 2–10 μm). Furthermore, because the scatter in the measurements of Fratini et al.[6] is substantially greater than that in the other data sets, we averaged adjacent pairs of particle bins to reduce this scatter.

1.1.1.3 Sow et al. (2009) data set

Sow et al.[7] used two optical particle counters at heights of 2.1 and 6.5 m to measure the size-resolved vertical flux of dust aerosols larger than 0.3 μm. They simultaneously measured the wind speed at several heights, which they used to obtain the dust flux through the gradient method of Gillette et al.[3]. Sow et al.[7] reported measurements made during three dust storms in Niger for which the average wind friction speed varied between 0.4 and 0.6 m/; they did not report the soil type.

1.1.1.4 Shao et al. (2011) data set

Shao, Ishizuka, and co-authors[8, 24] reported measurements of the vertical dust flux generated by a strong erosion event during the Japanese Australian Dust Experiment (JADE). The JADE field campaign took place in 2006 on a flat, fallow agricultural field with a loamy sand soil in southeastern Australia[24, 25]. The investigators used optical particle counters at 1.0, 2.0, and 3.5 m heights to measure the particle concentration in the 0.3–8.4 μm geometric diameter size range (Ishizuka, 2012, personal communication). Simultaneous wind speed measurements were made with anemometers at 0.50 and 2.16 m height. These measurements were combined to calculate the vertical dust flux as a function of friction velocity using the gradient method[3], with an added correction for the gravitational settling of dust particles. The measured

wind friction speed was in the range of <0.20 m/s to 0.55m/s. The authors questioned the reliability of the 0.3 – 0.6 μm size bin (p. 13 of Ref. [8]), which is thus not used here.

1.1.1.5 Rosenberg et al. (2014) data set

In contrast to the previous data sets, which were all obtained on the ground during active dust emission, the measurements of Rosenberg et al.[9] were made from an airplane flying over dusty regions in the central Sahara. The authors obtained measurements of the size-resolved aerosol fluxes up to 300 μm diameter for four different regions and at three different ranges of the vertical turbulent kinetic energy. Rosenberg et al. obtained these size-resolved aerosol fluxes using eddy covariance, which was facilitated by high frequency measurements of the size-resolved aerosol concentration (using several different OPCs) and the 3D wind (using pitot probes). These flux measurements were made in the lower portion of the atmospheric boundary layer, at altitudes ranging between ~100 – 1000 m. We only use the size-resolved aerosol flux measurements with particle sizes ≥ 0.5 μm because (i) measurements of the SAMUM campaign over the Sahara desert[26-28] showed that aerosols with diameter ≤ 0.5 μm are largely not dust aerosols[29], and (ii) the fraction of aerosols ≤ 0.5 μm that is dust is often coated in volatiles[26], which was not accounted for in Rosenberg et al.[9]. Conversely, we assume that the aerosol fluxes > 0.5 μm are entirely due to dust[26-28].

1.1.2 Obtaining the globally-averaged emitted dust PSD

After the previous section described the analysis of the emitted dust PSD data sets, we now describe the procedure that uses these data sets to determine the most likely globally-averaged emitted dust PSD and its 95% confidence interval. We obtain the most likely globally-averaged emitted dust size distribution using a statistical model that accounts for systematic errors inherent in each study's measurement methodology, which allows us to better constrain the emitted dust size distribution than otherwise possible. Specifically, we (i) fit each emitted dust PSD data set to an analytical function, (ii) use these analytical functions in a maximum likelihood procedure that explicitly consider the systematic errors between data sets, and (iii) use a bootstrap procedure [30, 31] to obtain the 95% confidence interval.

1.1.2.1 Fitting the emitted dust PSD

We thus first fit each data set to the analytical expression of the emitted dust PSD obtained from brittle fragmentation theory[10], which is in good agreement with each data set[9, 15]. This expression is given by

$$\frac{dV_{\text{emit}}}{d\ln D} = \frac{D}{c_{\text{V}}}\left[1+\text{erf}\left(\frac{\ln(D/D_{\text{M}})}{\sqrt{2}\ln\Omega_{\text{s}}}\right)\right]\exp\left[-\left(\frac{D}{\lambda}\right)^3\right], \quad \text{(S.2)}$$

where V_{emit} is the normalized volume concentration of emitted dust aerosols with geometric size D, c_{V} is a normalization constant, and Ω_{s}, D_{M}, and λ are model parameters whose significance are discusses in Ref. [10]. We used a non-linear least-squares analysis[23] to fit equation (S.2) to each data set, which yielded the least-squares estimates of the model parameters (Ω_{s}, D_{M}, and λ), their errors, and their covariances. Because systematic errors between data sets are much larger than the random errors within each data set (see discussion above), we assumed that the relative error, which is due to both random and systematic errors, is equal for all data points within a data set.

1.1.2.2 Using the maximum likelihood method to estimate the most likely globally-averaged emitted dust PSD

The above procedure thus yields five values of Ω_{s}, D_{M}, and λ, with their errors and covariances. We use these five estimates in a likelihood procedure to obtain the maximum likelihood estimates (MLEs) of the globally-representative values, $\tilde{\mu}_{\Omega_{\text{s}}}$, $\tilde{\mu}_{D_{\text{M}}}$, and $\tilde{\mu}_{\lambda}$, that describe the globally-averaged emitted dust PSD per equation (S.2). This procedure explicitly accounts for the systematic error affecting the five fitted values of Ω_{s}, D_{M}, and λ. That is, as we describe in more detail below, we assume that each data set's values of Ω_{s}, D_{M}, and λ are drawn from normal distributions for which the standard deviation represents

the average systematic errors τ_{Ω_s}, τ_{D_M}, and τ_λ between data sets. We then use maximum likelihood procedures to find both the globally-representative parameter values ($\tilde{\mu}_{\Omega_s}$,$\tilde{\mu}_{D_M}$, and $\tilde{\mu}_\lambda$) and the characteristic systematic error between data sets (τ_{Ω_s}, τ_{D_M}, and τ_λ), thereby propagating these errors into the uncertainty on the emitted dust size distribution (shaded region in Fig. 1c).

Procedure for obtaining $\tilde{\mu}_{\Omega_s}$ and $\tilde{\mu}_{D_M}$. Since Ω_s and D_M occur jointly inside the error function in equation (S.2), their values are correlated. Making the standard assumption of normally-distributed errors, we describe the likelihood of obtaining the fitted parameters $\Omega_{s,i}$ and $D_{M,i}$ with a bivariate normal distribution that is centered around the 'true' values $\mu_{\Omega_s,i}$ and $\mu_{D_M,i}$ *for the particular data set i*. That is, as the standard errors $\sigma_{\Omega_s,i}$ and $\sigma_{D_M,i}$ approach zero and equation (S.2) becomes a perfect to the measured data, $\Omega_{s,i}$ and $D_{M,i}$ respectively approach $\mu_{\Omega_s,i}$ and $\mu_{D_M,i}$.

The joint probability of $\Omega_{s,i}$ and $D_{M,i}$ is thus given by

$$\begin{pmatrix}\Omega_{s,i}\\ D_{M,i}\end{pmatrix} \sim N_2\left[\begin{pmatrix}\mu_{\Omega_s,i}\\ \mu_{D_M,i}\end{pmatrix}, \Sigma_i\right], \text{where} \tag{S.3}$$

$$\Sigma_i = \begin{pmatrix}\sigma^2_{\Omega_s,i} & \rho_i\sigma_{\Omega_s,i}\sigma_{D_M,i}\\ \rho_i\sigma_{\Omega_s,i}\sigma_{D_M,i} & \sigma^2_{D_M,i}\end{pmatrix} \tag{S.4}$$

where N_2 denotes a bivariate normal distribution, for which the first term in parentheses denotes the distribution's median, and the second term (Σ_i) the covariance matrix. Furthermore, ρ_i is the correlation between $\Omega_{s,i}$ and $D_{M,i}$ for the particular data set i; ρ_i, $\sigma_{\Omega_s,i}$, and $\sigma_{D_M,i}$ are obtained from the least-squares fitting procedure of equation (S.2) to data set i.

Even if all random error is eliminated from the measurements, systematic errors would cause the values of $\mu_{\Omega_s,i}$ and $\mu_{D_M,i}$ obtained for each of the five data sets to be offset from the 'true' $\tilde{\mu}_{\Omega_s}$ and $\tilde{\mu}_{D_M}$ that actually occur in the real world. Since differences in soil properties and wind speed seem to have only limited impact on the emitted dust PSD (see discussion above), we infer that these systematic errors are largely due to differences in experimental techniques[19]. We assume that the systematic errors for the five data sets are drawn from a bivariate normal distribution centered around zero, with unknown variances $\tau^2_{\Omega_s}$ and $\tau^2_{D_M}$, respectively, for Ω_s and D_M. That is,

$$\begin{pmatrix}\mu_{\Omega_s,i}\\ \mu_{D_M,i}\end{pmatrix} \sim N_2\left[\begin{pmatrix}\tilde{\mu}_{\Omega_s}\\ \tilde{\mu}_{D_M}\end{pmatrix}, \Gamma\right], \text{where} \tag{S.5}$$

$$\Gamma = \begin{pmatrix}\tau^2_{\Omega_s} & \eta\tau_{\Omega_s}\tau_{D_M}\\ \eta\tau_{\Omega_s}\tau_{D_M} & \tau^2_{D_M}\end{pmatrix}, \tag{S.6}$$

where η is the correlation between $\tilde{\mu}_{\Omega_s}$and $\tilde{\mu}_{D_M}$, which we estimate as the correlation between the 5 values of $\Omega_{s,i}$ and $D_{M,i}$, yielding η = 0.68. Combining equations (S.5) and (S.6) then yields

$$\begin{pmatrix}\Omega_{s,i}\\ D_{M,i}\end{pmatrix} \sim N_2\left[\begin{pmatrix}\tilde{\mu}_{\Omega_s}\\ \tilde{\mu}_{D_M}\end{pmatrix}, \Sigma_i + \Gamma\right] = \tag{S.7}$$

$$N_2\left[\begin{pmatrix}\tilde{\mu}_{\Omega_s}\\ \tilde{\mu}_{D_M}\end{pmatrix}, \begin{pmatrix}\sigma^2_{\Omega_s,i} + \tau^2_{\Omega_s} & \rho_i\sigma_{\Omega_s,i}\sigma_{D_M,i} + \eta\tau_{\Omega_s}\tau_{D_M}\\ \rho_i\sigma_{\Omega_s,i}\sigma_{D_M,i} + \eta\tau_{\Omega_s}\tau_{D_M} & \sigma^2_{D_M,i}+\tau^2_{D_M}\end{pmatrix}\right].$$

The likelihood of obtaining any particular set of $\Omega_{s,i}$ and $D_{M,i}$ values from the n = 5 data sets is then[23]

$$L = \prod_{i=1}^{n} N_2\left[\begin{pmatrix}\tilde{\mu}_{\Omega_s}\\ \tilde{\mu}_{D_M}\end{pmatrix}, \Sigma_i + \Gamma\right] = \prod_{i=1}^{n} \frac{1}{2\pi\sqrt{\left(\sigma^2_{\Omega_s,i} + \tau^2_{\Omega_s}\right)\left(\sigma^2_{D_M,i} + \tau^2_{D_M}\right)\left(1-r_i^2\right)}} \exp\left[-\frac{1}{2\left(1-r_i^2\right)} Q_i\left(\Omega_{s,i}, D_M\right)\right], \tag{S.8}$$

where

$$Q_i\left(\Omega_{s,i}, D_{M,i}\right) = \frac{\left(\Omega_{s,i} - \tilde{\mu}_{\Omega_s}\right)^2}{\sigma^2_{\Omega_s,i} + \tau^2_{\Omega_s}} + \frac{\left(D_{M,i} - \tilde{\mu}_{D_M}\right)^2}{\sigma^2_{D_M,i} + \tau^2_{D_M}} - 2r_i \frac{\left(\Omega_{s,i} - \tilde{\mu}_{\Omega_s}\right)\left(D_{M,i} - \tilde{\mu}_{D_M}\right)}{\sqrt{\sigma^2_{\Omega_s} + \tau^2_{\Omega_s}}\sqrt{\sigma^2_{D_M} + \tau^2_{D_M}}}, \tag{S.9}$$

and

$$r_i = \frac{\rho_i \sigma_{\Omega_s,i} \sigma_{D_M,i} + \eta \tau_{\Omega_s} \tau_{D_M}}{\sqrt{\sigma_{\Omega_s,i}^2 + \tau_{\Omega_s}^2} \sqrt{\sigma_{D_M,i}^2 + \tau_{D_M}^2}} \quad \text{(S.10)}$$

By maximizing the likelihood function L with the calculated values of $\Omega_{s,i}$ and $D_{M,i}$, we estimated the unknown parameters $\tilde{\mu}_{\Omega_s} = 2.10$, $\tilde{\mu}_{D_M} = 1.52$ μm, $\tau_{\Omega_s} = 0.25$, and $\tau_{D_M} = 0.54$ μm.

Procedure for obtaining $\tilde{\mu}_\lambda$. We now describe the procedure for obtaining the MLE of $\tilde{\mu}_\lambda$, which is similar to that for $\tilde{\mu}_{\Omega_s}$ and $\tilde{\mu}_{D_M}$ described above. $\tilde{\mu}_\lambda$ is the most likely globally-representative value of the parameter λ, which affects the shape of the size distribution curve for particle diameters $> \sim 10$ μm. Since Ω_s and D_M predominantly describe the size distribution for smaller particle sizes, λ is only weakly correlated to Ω_s and D_M. For simplicity, we thus consider the fitted parameter λ_i to be an independent parameter that is normally distributed (denoted by N) around the 'true' value μ_{λ_i} that exists for each *particular data set i*. The likelihood of obtaining the fitted parameter λ_i is then

$$\lambda_i \sim N(\mu_{\lambda_i}, \sigma_{\lambda_i}^2), \quad \text{(S.11)}$$

where the standard error σ_{λ_i} is obtained from the least-squares fitting procedure of equation (S.2) to the data set i. As with $\mu_{\Omega_s,i}$ and $\mu_{D_M,i}$, the value of μ_{λ_i} is affected by systematic errors that offset it from the 'true' $\tilde{\mu}_\lambda$ that actually occurs in the real world. We again assume that this systematic error is given by a normal distribution with zero mean and variance τ_λ^2. That is,

$$\mu_{\lambda_i} \sim N(\tilde{\mu}_\lambda, \tau_\lambda^2). \quad \text{(S.12)}$$

Combining equations (S.11) and (S.12) then yields the likelihood of obtaining the particular set of λ_i values from the $n = 5$ data sets:

$$L = \prod_{i=1}^{n} N\left(\tilde{\mu}_\lambda, \sigma_{\lambda,i}^2 + \tau_\lambda^2\right) = \prod_{i=1}^{n} \frac{1}{\sqrt{2\pi\left(\sigma_{\lambda,i}^2 + \tau_\lambda^2\right)}} \exp\left[-\frac{\left(\lambda_i - \tilde{\mu}_\lambda\right)^2}{2\left(\sigma_{\lambda,i}^2 + \tau_\lambda^2\right)}\right] \quad \text{(S.13)}$$

By again maximizing the likelihood function L, we estimated the unknown parameters $\tilde{\mu}_\lambda = 20.5$ μm and $\tau_\lambda = 7.9$ μm.

After calculating $\tilde{\mu}_{\Omega_s}$, $\tilde{\mu}_{D_M}$, and $\tilde{\mu}_\lambda$ through the above procedures, we used these values to calculate the normalization factor c_V by forcing the integral over equation (S.2), from $D = 0.2$ to 20 μm, to unity. The resulting most likely globally-averaged emitted dust size distribution is plotted in Figure 1c.

1.1.2.3 Obtaining the error in the globally-averaged emitted dust size distribution

In addition to obtaining the most likely globally-averaged emitted dust size distribution, we also require its 95% confidence interval. We obtained this using a modified bootstrap procedure[30, 31]:

1. We randomly choose one data set from the total of five emitted dust PSD data sets, and repeat this five times with resampling. This results in a set of five randomly-selected data sets, in which each data set can be represented more than once, or not at all. Note that, since the bootstrapping method requires identical and independently distributed measurements[30, 31], we thus necessarily assume that all data sets are independent. This is another reason for combining the three Gillette studies into a single data set.
2. We obtain the values of $\tilde{\mu}_{\Omega_s}$, $\tilde{\mu}_{D_M}$, and $\tilde{\mu}_\lambda$ from the procedure described in Section 1.1.2.2.
3. We repeat steps 1 and 2 a large number of times, yielding a large number of possible curves for the globally-averaged emitted dust PSD.
4. For each value of the particle diameter D, the 95% confidence interval is the interval within which 95% of the curves obtained in step 3 lie[30, 31]. This confidence interval is plotted as gray shading on Figure 1c.

1.2 Analysis of the globally-averaged and size-resolved dust lifetime

We constrain the globally averaged size-resolved dust lifetime from the lifetime simulated with nine different climate and chemical transport models. These include GISS (see figure S12 in Ref. [32]), GMOD (see table 2 in Ref. [33]), CESM (calculated from simulations reported in Ref. [34]), MOZART (see Table 2 in Ref. [35]), UMI (see table 3 in [36]; our Fig.2 shows the geometric mean of the three reported simulations with different meteorological data sets), MERRAero (calculated from simulations accessible at http://opendap.nccs.nasa.gov/dods/GEOS-5/MERRAero[37, 38-40]), WRF-Chem (see Section 5.1), GEOS-Chem (Section 5.2), and HadGEM (Section 5.3). We use the results of these nine global transport models to constrain the size-resolved dust lifetime in a manner similar to that described above for the emitted dust PSD. That is, first we fit each model result with an analytical function (Section 1.2.1), after which we obtain the most likely globally-averaged size-resolved dust lifetime using the maximum likelihood method (Section 1.2.2), and finally we obtain the 95% confidence interval using the bootstrap method (Section 1.2.3).

1.2.1 Fitting the size-resolved dust lifetime

The nine simulation results indicate that the dust lifetime decreases approximately exponentially with particle size (see Fig. 1d):

$$T(D) = T_0 \exp\left(-D / D_{\text{dep}}\right), \tag{S.14}$$

where T_0 is the lifetime of dust with vanishingly small diameter, which is of the order of 10 days (Fig. 1d), and the constant D_{dep} scales the exponential decay of the dust lifetime with particle size. Equation (S.14) can be written as

$$\ln(T) = a + bD, \tag{S.15}$$

where $a = \ln(T_0)$ and $b = -1/D_{\text{dep}}$. For a given model *i*, we used a linear least-squares procedure to fit equation (S.15) to the model results. This yielded the intercept a_i and slope b_i, the correlation ρ_i between intercept and slope, and the errors in the intercept ($\sigma_{a,i}$) and slope ($\sigma_{b,i}$) relative to the 'true' values of the intercept ($\mu_{a,i}$) and slope ($\mu_{b,i}$) *for the particular climate model i*. These errors are caused by internal model error, the finite extent of particle bins, the fact that equation (S.14) is a theoretical and not exact description of the lifetime dependence on particle size, and other sources of error.

1.2.2 Using the maximum likelihood method to obtain the most likely globally-averaged dust lifetime

We used these nine estimates of a_i and b_i in a maximum likelihood procedure to obtain the most likely globally-representative values of $\tilde{\mu}_{T_0}$ and $\tilde{\mu}_{D_{dep}}$, which describe the globally-averaged dust lifetime per equation (S.15). Because the slope and intercept of a least-squares fit are correlated[23], we again describe the joint probability of obtaining the intercept a_i and slope b_i in equation (S.15) using a bivariate normal distribution, which is centered around the 'true' values $\mu_{a,i}$ and $\mu_{b,i}$:

$$\begin{pmatrix} a_i \\ b_i \end{pmatrix} \sim N_2\left[\begin{pmatrix} \mu_{a,i} \\ \mu_{b,i} \end{pmatrix}, \Sigma_i\right], \text{ where} \tag{S.16}$$

$$\Sigma_i = \begin{pmatrix} \sigma_{a,i}^2 & \rho_i \sigma_{a,i} \sigma_{b,i} \\ \rho_i \sigma_{a,i} \sigma_{b,i} & \sigma_{b,i}^2 \end{pmatrix}. \tag{S.17}$$

The values of $\mu_{a,i}$ and $\mu_{b,i}$ for each climate model are affected by systematic biases, for instance due to errors in the deposition scheme[41], that offset them from the 'true' (unbiased) intercept $\tilde{\mu}_a$ and slope $\tilde{\mu}_b$ that actually occur in the real world. Similar to our procedure for constraining the emitted dust PSD (Section 1.1.2), we assume that these systematic errors are drawn from a bivariate normal distribution centered around zero, and with unknown variances τ_a^2 and τ_b^2, respectively, for a and b. That is,

$$\begin{pmatrix} \mu_{a,i} \\ \mu_{b,i} \end{pmatrix} \sim N_2\left[\begin{pmatrix} \tilde{\mu}_a \\ \tilde{\mu}_b \end{pmatrix}, \Gamma\right], \text{ where} \tag{S.18}$$

$$\Gamma = \begin{pmatrix} \tau_a^2 & \eta \tau_a \tau_b \\ \eta \tau_a \tau_b & \tau_b^2 \end{pmatrix} \tag{S.19}$$

where η = -0.75 is the correlation between $\mu_{a,i}$ and $\mu_{b,i}$. Combining equations (S.18) and (S.19) then yields the joint probability distribution of a_i and b_i in terms of their 'true' globally-representative values ($\tilde{\mu}_a$ and $\tilde{\mu}_b$), their mean variance (τ_a^2 and τ_b^2), and the standard errors ($\sigma_{a,i}^2$ and $\sigma_{b,i}^2$) and covariances (ρ_i) obtained from the least-squares fitting procedure of equation (S.15) to data set *i*:

$$\begin{pmatrix} a_i \\ b_i \end{pmatrix} \sim N_2\left[\begin{pmatrix} \tilde{\mu}_a \\ \tilde{\mu}_b \end{pmatrix}, \Sigma_i + \Gamma\right] = N_2\left[\begin{pmatrix} \tilde{\mu}_a \\ \tilde{\mu}_b \end{pmatrix}, \begin{pmatrix} \sigma_{a,i}^2 + \tau_a^2 & \rho_i \sigma_{a,i}\sigma_{b,i} + \eta\tau_a\tau_b \\ \rho_i \sigma_{a,i}\sigma_{b,i} + \eta\tau_a\tau_b & \sigma_{a,i}^2 + \tau_b^2 \end{pmatrix}\right]. \quad \text{(S.20)}$$

The likelihood of obtaining the particular set of intercepts and slopes from the n = 9 climate model results is then

$$L = \prod_{i=1}^{n} N_2\left[\begin{pmatrix} \tilde{\mu}_a \\ \tilde{\mu}_b \end{pmatrix}, \Sigma_i + \Gamma\right] = \prod_{i=1}^{n} \frac{1}{2\pi\sqrt{\sigma_{a,i}^2 + \tau_a^2}\sqrt{\sigma_{b,i}^2 + \tau_b^2}\sqrt{1 - r_i^2}} \exp\left[-\frac{1}{2\left(1 - r_i^2\right)} Q_i\left(a_i, b_i\right)\right], \quad \text{(S.21)}$$

where

$$Q_i\left(a_i, b_i\right) = \frac{\left(a_i - \tilde{\mu}_a\right)^2}{\sigma_{a,i}^2 + \tau_a^2} + \frac{\left(b_i - \tilde{\mu}_b\right)^2}{\sigma_{b,i}^2 + \tau_b^2} - 2r_i \frac{a_i - \tilde{\mu}_a}{\sqrt{\sigma_a^2 + \tau_a^2}} \frac{b_i - \tilde{\mu}_b}{\sqrt{\sigma_b^2 + \tau_b^2}}, \quad \text{(S.22)}$$

and

$$r_i = \frac{\rho_i \sigma_{a,i}\sigma_{b,i} + \eta\tau_a\tau_b}{\sqrt{\sigma_{a,i}^2 + \tau_a^2}\sqrt{\sigma_{b,i}^2 + \tau_b^2}}. \quad \text{(S.23)}$$

We obtained the parameters $\tilde{\mu}_a$ = 2.5, $\tilde{\mu}_b$ = -0.22, τ_a = 0.41, and τ_b = 0.03 by maximizing the likelihood function L[42], which yield $\tilde{\mu}_{T_0}$ = 12.5 days, $\tilde{\mu}_{D_{dep}}$ = 4.6 days, τ_{T_0} = 5.1 days, and $\tau_{D_{dep}}$ = 0.7 days. The resulting most likely globally-averaged dust lifetime is plotted on Figure 1d.

1.2.3 Obtaining the error in the globally-averaged dust lifetime

In addition to obtaining the most likely size-resolved dust lifetime, we also require its uncertainty. We obtained this using a modified bootstrap procedure[30, 31] similar to what we used for the emitted dust PSD (Section 1.1.2.3):

1. We randomly chose one data set from the total of nine dust lifetime data sets, and repeat this nine times with resampling. This resulted in a set of nine randomly-selected data sets, in which each data set can be represented more than once, or not at all.
2. We obtained the values of $\tilde{\mu}_a$ and $\tilde{\mu}_b$ from the procedure described above.
3. We repeated steps 1 and 2 a large number (i.e., 10^5) of times, yielding a large number of possible curves for the globally-averaged dust lifetime.
4. For each value of the particle diameter *D*, the 95% confidence interval is the interval within which 95% of the curves obtained in step 2 lie[30, 31]. This confidence interval is plotted as gray shading on Figure 1d.

1.3 Obtaining the globally-averaged dust size distribution and its uncertainty

With both the MLEs of the globally-averaged emitted dust PSD (Section 1.1) and dust lifetime (Section 1.2) known, we inserted these results into equation (3) to obtain the most likely globally-averaged normalized atmospheric dust PSD (dashed line in Fig. 2a). Furthermore, the bootstrap procedures in Sections 1.1 and 1.2 yield a large number of possible curves for the emitted dust PSD and the size-resolved dust lifetime. Using equation (3), we use these to similarly generate a large number (i.e., 10^5) of curves for the size-resolved globally-averaged dust size distribution. The plotted 95% confidence interval (gray shading) is the interval within which 95% of the ensemble values lie[30, 31]. We find that the volume size distribution of atmospheric dust peaks around 5 μm (Fig. 2a), which is slightly coarser than a compilation of ground-based measurements[16].

1.4 Analysis of atmospheric size distribution in models

Figure 2 shows the most likely atmospheric dust size distribution and its uncertainty. For comparison, we also show the atmospheric dust size distribution reported by seven climate and chemical transport models that participated in the Aerosol Comparison between Observations and Models (AeroCom) project[43]. Specifically, the models included in Fig. 2 are: CAM (see Table 2 in Ref. [44]), the GISS ModelE (Figure 2 in Ref. [2]), GOCART (see table 3 in Ref. [45]), MATCH (see table 8 in Ref. [46]), MOZART (see Table 2 in Ref. [35]), UMI (see table 3 in Ref. [36]; our Fig.2 shows the geometric mean of the three reported simulations with different meteorological data sets), and LOA (see tables 2 and 3 in Ref. [47]). We were unable to locate literature reporting atmospheric dust size distribution for other AeroCom models (SPRINTARS[48-50]; ECMFW[51], UIO_CTM[52, 53]; LSCE[54]; ECHAM5-HAM[55]; MIRAGE[56]; TM5[57, 58]).

2. Analysis of the shortwave extinction efficiency

We seek to obtain the dust optical depth per unit dust loading that is produced by the globally-averaged atmospheric size distribution (Section 1). To do so, we require $Q_{ext}(D)$, the globally-averaged extinction efficiency of dust as a function of its particle size, at the wavelength of 550 nm for which the global DAOD is constrained[59]. The extinction efficiency depends on the size, shape, and refractive index of dust aerosols. We thus used measurements to constrain the globally-averaged dust index of refraction (Section 2.1) and dust particle shape (Section 2.2), which we then converted to $Q_{ext}(D)$ using the single-scattering database of Meng et al.[60] (Section 2.3).

2.1 Globally-averaged dust index of refraction

Measurements of the real refractive index of dust at 550 nm from a variety of source regions and at a range of transport stages (i.e., fresh versus aged dust) are in the approximate range of $m = 1.45 – 1.60$ [17, 27, 28, 61-69], such that we take the globally-averaged real index of refraction as $n = 1.53 \pm 0.03$. This value is thus intended to account for changes in n during transport due to chemical processing, which might be important for Asian dust[68], but is likely less important for African dust[61, 70]. Note that, by characterizing the global ensemble of dust aerosols with a single average value for the index of refraction, rather than with a distribution as we do with the shape (see below), we are neglecting any non-linearities in the extinction efficiency with refractive index. Because the dependence of extinction on the real refractive index in the relatively narrow range of 1.45-1.60 is largely linear[60], the error from this simplification is small compared to other errors in our analysis. Indeed, a sensitivity study indicates that the error associated with this simplification is less than a percent.

Whereas the real refractive index of dust is thus relatively well-known, the imaginary refractive index reported by many in situ studies[61, 71-73] is substantially larger than that derived from (ground-based or satellite) remote sensing observations[62, 63, 74]. In order to encompass both, we take $^{10}\log(-k) = -2.5 \pm 0.3$. However, since even large variability in the imaginary refractive index has a limited effect on the dust extinction efficiency[75, 76], this large uncertainty in the dust absorption properties does not contribute substantially to the uncertainty in the global dust loading.

2.2 Globally-averaged distribution of dust particle shapes

Since the uncertainty in dust optical properties produces only limited uncertainty in the extinction efficiency, the main uncertainty in $Q_{ext}(D)$ arises from the irregular shape of dust particles. A range of experimental studies have used electron microscopy to quantify the irregularity of dust particles. Most of these studies focused on measuring the aspect ratio of the particle, that is, the ratio of the particle's major axis to its minor axis; the latter of these is usually obtained by fitting an ellipse to the particle and deriving the perpendicular dimension by requiring that the ellipsoid area equals that of the projected particle[72, 77]. These measurements indicate that the probability distribution function of the deviation of the aspect ratio from 1 (i.e., a perfect sphere) is well-described as a lognormal function[72]. Measurements show that the median aspect ratio is in the range of 1.5 to 1.9, and the geometric standard deviation is approximately 0.6; both parameters are insensitive to particle size, although there's an increasing trend in aspect ratio with transport distance due to the preferential settling of spherical dust[27, 72, 77-83]. There are far fewer measurements of the particle's third dimension, its height; the only extensive quantitative

measurements were reported by Okada et al.[78]. They performed electron microscopy on dust sampled in China, and found that the ratio of particle height to minor axis is lognormally distributed, with a median of about 1/3. They also found only small variations in the average height-to-width ratio with particle size (see their Fig. 1b), and no clear relationship between aspect ratio and height-to-width ratio. Chou et al.[79] also reported a height to major axis ratio of about one third, and Veghte and Freedman[84] reported values ranging between 0.1 to 0.8 for different minerals.

Based on the measurements reviewed above, we describe the dust particle shape as a tri-axial ellipsoid[60], with the deviation of the aspect ratio (AR) from 1 (spherical) described by a lognormal function[72] with a median aspect ratio of $\overline{\varepsilon_a}$ = 1.7 ± 0.2 and a geometric standard deviation of σ_{ε_a} = 0.6 ± 0.2. That is,

$$P(AR) = \frac{1}{\sqrt{2\pi}\sigma_{\varepsilon_a}(AR-1)} \exp\left[-0.5 \left(\frac{\ln(AR-1) - \ln(\overline{\varepsilon_a} - 1)}{\sigma_{\varepsilon_a}} \right)^2 \right]. \quad \text{(S.24)}$$

The treatment of the dust particle height is impeded by two factors. First, there is only one detailed quantitative study of the probability distribution of dust particle heights[78], which also was taken of Asian dust rather than the globally more important North African dust. Second, the presence of very aspherical dust aerosols suggested by this study is difficult to account for, because the optical properties of highly aspherical particles are difficult to calculate and thus very uncertain[85-88], and are consequently not included in the Meng et al.[60] single-scattering database. We therefore cannot realistically account for the distribution of particle heights, or its uncertainty, and instead take the height-to-length ratio as $\overline{\varepsilon_h}$ = 0.333, based on the limited available measurements[78, 79, 84].

Note that we assume dust particles are randomly oriented[85], and that we cannot account for microscale roughness and thus have to assume dust particles are smooth.

2.3 Obtaining the globally-averaged extinction efficiency and its uncertainty

We use the single-scattering database of Meng et al.[60] to convert the globally-averaged dust index of refraction and the ensemble of dust particle shapes to an ensemble of extinction efficiencies. We then take $Q_{ext}(D)$ as the average extinction efficiency of dust particles in this ensemble with a given geometric diameter D. For reference, we also calculated the extinction efficiency of spherical dust particles from Mie theory[89] and included both curves in Figure 1b. As expected, the non-spherical shape of dust aerosols substantially increases their extinction efficiency over the case of spherical particles[85, 90].

To obtain the uncertainty in $Q_{ext}(D)$, we assumed that each of the parameters describing the refractive index of dust and the distribution of shapes is independent. This allowed us to obtain a large number of parameters sets by randomly choosing values from the normal distribution defined by the mean and standard error of each parameter as given above (n = 1.53 ± 0.03; log(-k) = -2.5 ± 0.3; $\overline{\varepsilon_a}$ = 1.7 ± 0.3 , and σ_{ε_a} = 0.6 ± 0.2). We then used the single-scattering database of Meng et al.[60] to convert each set of parameters to a curve of $Q_{ext}(D)$, yielding a large number (i.e., 10^5) of realizations of $Q_{ext}(D)$. We obtained the 95% confidence interval as the range within which 95% of these functions fall, which is given as the gray shading in Figure 1b. This confidence interval thus captures the uncertainty in the globally-averaged extinction efficiency due to the experimental uncertainty in the dust optical properties and in the probability distribution for the dust particle shape, as a function of dust geometric diameter.

3. Constraining the size-resolved global dust emission rate, loading, and DAOD

The previous sections described the procedure for constraining the globally-averaged dust PSD and extinction efficiency. Equations (1)-(4) combine these with constraints on the global dust aerosol optical depth (DAOD) from our companion study[59], yielding the size-resolved global atmospheric dust emission rate, and atmospheric mass loading $\frac{dM_{\mathrm{atm}}}{dD}$ (Fig. 2b). Furthermore, the integrals over these quantities yield

the global dust emission rate F_{emit} (Fig. 3a) and mass loading L_{atm} (Fig. 3b). We also calculate the size-resolved DAOD from Eq. (2), yielding

$$\frac{d\tau_{\text{d}}}{dD} = \frac{L_{\text{atm}}}{\text{A}_{\text{Earth}}} \frac{dV_{\text{atm}}}{dD} \frac{A(D)}{M(D)} Q_{\text{ext}}(D) \cdot \tag{S.25}$$

However, in order to use the analytical framework of equations (1)-(4) to constrain these quantities, we need to propagate the uncertainties in the various physical parameters and analytical functions. Due to the complexity of these analytical functions, the covariance of their parameters, and their occurrence inside of integrals, we cannot parametrically estimate the uncertainty on the desired quantities. We thus instead obtain their probability distribution functions (pdfs) using a non-parametric method based on the bootstrap method[30, 31], which is similar to the procedures described in Sections 1.1.2.3, 1.2.3, 1.3, and 2.3. Indeed, the procedures above have yielded a large number of parameter sets for each of the functions used in Eqs. (1)–(4), namely for the globally-averaged size-resolved dust PSD ($\frac{dV_{\text{atm}}}{dD}$; see Section 1.3), the extinction efficiency ($Q_{\text{ext}}(D)$; see Section 2.3), and the dust lifetime ($T(D)$; see Section 1.2.3). Since these parameter sets are independent and identically distributed, we can apply the bootstrap technique to obtain pdfs of $\frac{dM_{\text{atm}}(D)}{dD}$, $\frac{d\tau_{\text{d}}(D)}{dD}$, L_{atm}, and F_{emit}. Specifically, we obtained these pdfs as follows:

1. We randomly selected a set of parameters from the bootstrap procedure performed on the functions $\frac{dV_{atm}}{dD}$, $Q_{\text{ext}}(D)$, and $T(D)$.
2. We randomly assigned a value to the dust density from the normal distribution defined by its mean and standard error [$\rho_{\text{d}} = (2.5 \pm 0.2) \cdot 10^3$ kg/m^3].
3. We used equations (2) – (4) to calculate the value of ε_{τ}.
4. We randomly chose a value of τ_{d} from its probability distribution obtained in Ridley et al.[59].
5. We used equation (1) to obtain L_{atm}.
6. We used that $\bar{T} = L_{\text{atm}}/F_{\text{emit}}$ to obtain F_{emit}.
7. We used the value of L_{atm} to obtain $\frac{dM_{\text{atm}}}{dD} = L_{\text{atm}} \frac{dV_{\text{atm}}}{dD}$.
8. We used Eq. (S.25) to obtain $\frac{d\tau_d}{dD}$.
9. We repeated the procedure in steps 1-8 a large number of times (i.e., 10^5).

Since the resulting distribution of values of $\frac{dM_{\text{atm}}(D)}{dD}$, $\frac{d\tau_{\text{d}}(D)}{dD}$, L_{atm}, and F_{emit} correspond to their probability distributions[30, 31], we obtained the 95% confidence intervals from the range in which 95% of the obtained values lie (grey shading in Fig. 2 and blue shading in Fig. 3).

4. Constraining the dust direct radiative effect (DRE)

The dust direct radiative effect is generated by extinction of radiation. It therefore is closely connected to the globally-averaged dust aerosol optical depth τ_{d} (e.g., Ref. [91]), which is a measure of the global extinction of SW radiation by dust. Consequently, we constrain the dust DRE by combining results on the size-resolved DAOD (Fig. 2c) with simulations of the efficiency with which this extinction produces DRE at top-of-atmosphere (TOA). Specifically, we have that

$$\zeta = \zeta_{\text{SW}} + \zeta_{\text{LW}} = \int_0^{D_{\text{max}}} \frac{d\tau_{\text{d}}}{dD} \Omega_{\text{SW}}(D) dD + \int_0^{D_{\text{max}}} \frac{d\tau_{\text{d}}}{dD} \Omega_{\text{LW}}(D) dD\,, \tag{S.26}$$

where ζ_{SW} and ζ_{LW} denote the SW and LW contributions to the total DRE (ζ), and the radiative effect efficiencies $\Omega_{\text{SW}}(D) = \frac{d\zeta_{\text{SW}}}{d\tau_{\text{d}}}$ and $\Omega_{\text{LW}}(D) = \frac{d\zeta_{\text{LW}}}{d\tau_{\text{d}}}$ are the all sky DRE that dust of diameter D produces per unit DAOD, due to interactions with SW and LW radiation, respectively.

The values of $\Omega_{\text{SW}}(D)$ and $\Omega_{\text{LW}}(D)$ depend on numerous factors, including the spatial and temporal variability of dust, the surface albedo and surface emissivity, the vertical temperature profile, the distribution of radiatively-active species such as clouds and greenhouse gases, and the asymmetry parameter and single-scattering albedo of dust. We thus require global model simulations to estimate

$\Omega_{\mathrm{SW}}(D)$ and $\Omega_{\mathrm{LW}}(D)$, for which we use results from four leading global models, namely CESM, GISS, GEOS-Chem, and WRF-Chem (see Fig. S3). The CESM simulations are described in Kok et al.[34], with dust optical properties from Albani et al.[92], and the methodology for obtaining the radiative effects for each particle bin are described in Conley et al.[93]. The GISS simulations are described in Miller et al.[2] (see especially their Fig. 2), and the WRF-Chem and GEOS-Chem simulations are described in Sections 5.1 and 5.2, respectively. All simulations use dust absorption properties that are consistent with recent findings that dust is less absorptive in the SW spectrum than previously thought[74, 94, 95].

Most global models unfortunately do not account for the radiative effects of scattering of LW radiation[1]. At TOA, the DRE from LW scattering likely accounts for about half[1] of the total LW DRE for a variety of standard clear-sky conditions. However, we follow the conservative treatment of Miller et al.[2] in assuming that LW scattering enhances the radiative effect from LW absorption by a factor of $\beta_{\mathrm{LW,scat}}$ = 0.3, thus accounting for only 23% of the LW DRE at TOA. As such, the constraints on LW warming by dust obtained here should be seen as conservative.

We discretize Eq. (S.26) to obtain the SW ($\chi_{i,k,\mathrm{SW}}$) and LW ($\chi_{i,k,\mathrm{LW}}$) DRE for each particle bin *k* for each of the four global model simulations *i*:

$$\chi_{i,k,\mathrm{SW}} = \Omega_{i,\mathrm{SW}}\left(D_{i,k}\right)\int_{D_{i,k-}}^{D_{i,k+}} \frac{d\tau_d}{dD}\,dD = \Omega_{i,\mathrm{SW}}\left(D_{i,k}\right)\Delta\tau_{\mathrm{d},i,k}\,, \tag{S.27a}$$

$$\chi_{i,k,\mathrm{LW}} = \left(1+\beta_{\mathrm{LW,scat}}\right)\Omega_{i,\mathrm{LW}}\left(D_{i,k}\right)\int_{D_{i,k-}}^{D_{i,k+}} \frac{d\tau_d}{dD}\,dD = \left(1+\beta_{\mathrm{LW,scat}}\right)\Omega_{i,\mathrm{LW}}\left(D_{i,k}\right)\Delta\tau_{\mathrm{d},i,k}\,, \tag{S.27b}$$

where the index *k* sums over the particle bins of global model simulation *i*, $D_{i,k-}$ and $D_{i,k+}$ are respectively the lower and upper limits of particle size bin *k* of global model *i*, , and $\Delta\tau_{\mathrm{d},i,k}$ denotes the global optical depth produced by dust in the size range spanned by particle bin *k* in model *i*. The DRE in the SW and LW spectra is then the sum of that for the individual particle bins:

$$\zeta_{i,\mathrm{SW}} = \sum_k \chi_{i,k,\mathrm{SW}} + \Omega_{i,\mathrm{SW}}\left(D_{\max}\right)\int_{D_{\mathrm{lim},i}}^{D_{\max}} \frac{d\tau_d}{dD}\,dD\,, \text{ and} \tag{S.28a}$$

$$\zeta_{i,\mathrm{LW}} = \sum_k \chi_{i,k,\mathrm{LW}} + \left(1+\beta_{\mathrm{LW,scat}}\right)\Omega_{i,\mathrm{LW}}\left(D_{\max}\right)\int_{D_{\mathrm{lim},i}}^{D_{\max}} \frac{d\tau_d}{dD}\,dD\,. \tag{S.28b}$$

Since the global model simulations do not extend fully to $D_{\max}$ = 20 μm, the second term on the right-hand side of Eq. (S.28) accounts for the DRE produced by dust with diameters ranging from the upper size limit accounted for by global model *i* ($D_{\mathrm{lim},i}$) to $D_{\max}$. We obtain the values of $\Omega_{\mathrm{SW}}(D_{\max})$ and $\Omega_{\mathrm{LW}}(D_{\max})$ by extrapolating the model results for smaller particle sizes (Fig. S3), thereby estimating both at 20 ± 8 $\mathrm{Wm^{-2}}/\tau_{\mathrm{d}}$. Our results indicate that the global DRE due to dust with D > 20 μm is negligible (see Fig. S4), though it could still be important on local and regional scales.

4.1 Calculating the DRE using size-resolved DAOD from AeroCom simulations

We aim to use Eqs. (S.27, S.28) to compute the DRE that would be produced by the atmospheric dust size distribution simulated by the seven AeroCom models (colored lines in Fig. 2b). To do so, we require the optical depth $\Delta\tau^{j}_{\mathrm{d},i,k}$ that the mass size distribution of AeroCom model *j* would yield for particle bin *k* of global model *i*. We calculated $\Delta\tau^{j}_{\mathrm{d},i,k}$ as follows[96, 97]

$$\Delta\tau^{j}_{\mathrm{d},i,k} = \frac{1}{A_{\mathrm{Earth}}}\int_{D_{i,k-}}^{D_{i,k+}} \frac{dM_j}{dD}\frac{A(D)}{M(D)}Q_{\mathrm{ext,sph}}(D)\,dD\,, \tag{S.29}$$

where the surface area-to-mass ratio $A(D)/M(D) = 3/2\rho_{\mathrm{d}}D$ (see Eq. 2). We obtained the mass size distribution for AeroCom model *j*, $\frac{dM_j}{dD}$, by fitting power laws between the individual values of $\frac{dM_j}{dD}$ given by each particle bin; these power laws correspond to the solid colored lines in Fig. 2b. The extinction coefficient $Q_{\mathrm{ext,sph}}$ was taken as that of spherical dust, consistent with the assumption of spherical dust made in AeroCom models[2, 44-46], and thus calculated with Mie theory (brown line in Fig. 1b). To ensure that the results are consistent with reported AeroCom results, we normalized the sum of the optical depths

of the particle bins with the total optical depth $\tau_{d,j}$ for the AeroCom model j, given in Table 3 of Huneeus et al.[98]. That is,

$$\Delta\tau'^{j}_{d,i,k} = \Delta\tau^{j}_{d,i,k} \frac{\sum_k \Delta\tau^{j}_{d,i,k}}{\tau_{d,j}} \quad \text{(S.30)}$$

where $\Delta\tau'^{j}_{d,i,k}$ is the normalized optical depth for each particle bin. We inserted $\Delta\tau'^{j}_{d,i,k}$ into Eq. (S.27) to calculate the DRE for each particle bin of each combination of global model i and AeroCom model j. These results are shown in Figs. S4a-d for the four global models CESM, GISS, GEOS-Chem, and WRF-Chem; the error bars in these figures represent the spread from using $\Delta\tau'^{j}_{d,i,k}$ from the seven AeroCom models. We also use a similar procedure to Eqs. (S.29) and (S.30) to calculate the size-resolved dust optical depth (i.e., $d\tau'_d/dD$) for each AeroCom model, which is plotted in Fig. 2c.

We combined the above procedure with Eq. (S.28) to obtain a total of 28 estimates of the total TOA dust DRE, which resulted from the combination of seven AeroCom models with four global model calculations of $\Omega(D)$. Fig. 4 shows the median of these 28 values and the 95% CI, which we estimated from the range of the 26 values remaining after eliminating the two extreme values. Fig. 4 also shows six published estimates of DRE from AeroCom models[2, 74, 95, 99], although two of the three estimates in Forster et al.[95] include the SW radiative effect only.

4.2 Calculating the DRE using this study's constraints on the size-resolved DAOD

In addition to using the size-resolved dust loading from AeroCom simulations to calculate the dust DRE, we use the constraints on $\Delta\tau_{d,i,k}$ from our analysis (see Figs. 2c and S1c) to calculate the DRE. Specifically, we inserted a large number (10^5) of realizations of $\Delta\tau_{d,i,k}$ (see Section 3) into Eq. (S.27) to obtain the pdfs of $\chi_{i,k,\mathrm{SW}}$ and $\chi_{i,k,\mathrm{LW}}$, for which the median and the 95% CI are plotted in Figs. S4e-h. The difference of the radiative effect per particle bin with those calculated using the size-resolved dust loading from AeroCom models is shown in Figs. S4i-l. We then inserted these 10^5 realizations of $\chi_{i,k,\mathrm{SW}}$ and $\chi_{i,k,\mathrm{LW}}$ into Eq. (S.28) to obtain the pdfs of $\zeta_{i,\mathrm{SW}}$ and $\zeta_{i,\mathrm{LW}}$ (see Figs. S5a, b). Finally, we used $\zeta_{i,\mathrm{SW}}$ and $\zeta_{i,\mathrm{LW}}$ in the following procedure to obtain the pdf of the total DRE (ζ):

1. Obtain a realization of $\frac{d\tau_d}{dD}$ (see Section 3).
2. Randomly pick one of the four global models providing $\Omega_{\mathrm{SW}}(D)$ (Fig. S3a) and randomly select a corresponding realization of ζ_{SW}.
3. Randomly pick one of the four global models providing $\Omega_{\mathrm{LW}}(D)$ (Fig. S3b) and randomly select a corresponding realization of ζ_{LW}.
4. Obtain a realization of the total DRE from $\zeta = \zeta_{\mathrm{SW}} + \zeta_{\mathrm{LW}}$.
5. Repeat steps 1-4 a large number of times (10^5) to obtain the pdf of ζ, which is plotted in Fig. S5c.

We report the median and 95% CI of the probability distributions of ζ_{SW}, ζ_{LW}, and ζ in Fig. 4.

5. Global transport model simulations

To supplement the size-resolved dust lifetimes that have been reported in the literature[32-36, 40], we performed simulations with a number of leading global transport and climate models, namely WRF-Chem, GEOS-Chem, and HadGEM. Simulations with the first two models were also used to supplement the size-resolved radiative effect efficiencies obtained from previously-reported simulations with CESM[34] and GISS[2]. We describe the simulations with these three models below.

5.1 Description of WRF-Chem simulations

We used WRF-Chem version 3.5.1, updated by the Pacific Northwest National Laboratory (PNNL), to simulate the dust aerosol lifetime (Fig. 1d) and the size-resolved radiative effect efficiency (Fig. S3), averaged over the years 2004-2008. Our simulations used the MOSAIC (Model for Simulation Aerosol Interactions and Chemistry) aerosol module[100] coupled with the CBM-Z (carbon bond mechanism) photochemical mechanism[101]. The MOSAIC aerosol scheme uses the sectional approach to represent aerosol size distributions with eight discrete size bins[102], extending to 10 μm diameter. All major aerosol components, including sulfate (SO_4^{-2}), nitrate (NO_3^-), ammonium (NH_4^+), black carbon (BC), organic

matter (OM), sea-salt, methanesulfonic acid, and mineral dust are simulated in the model. The MOSAIC aerosol scheme includes physical and chemical processes of nucleation, condensation, coagulation, aqueous phase chemistry, and water uptake by aerosols. The treatment of dry and wet deposition processes are described in Refs. [103, 104].

In WRF-Chem, aerosol optical properties such as extinction, single-scattering albedo (SSA), and asymmetry factor for scattering are computed as a function of wavelength for each model grid box. Aerosols are assumed internally mixed in each bin, i.e., a complex refractive index is calculated by volume averaging for each bin for each chemical constituent of aerosols. The Optical Properties of Aerosols and Clouds (OPAC) dataset[105] is used for the SW and LW refractive indices of aerosols, except that a constant value of 1.53+0.003i is used for the SW refractive index of dust following Zhao et al.[106, 107], which is consistent with recent insights[62, 63, 74, 94]. A detailed description of the computation of aerosol optical properties in WRF-Chem can be found in Fast et al.[102] and Barnard et al.[108]. Aerosol radiative feedback is coupled with the Rapid Radiative Transfer Model (RRTMG)[109, 110] for both shortwave (SW) and longwave (LW) radiation[107]. Since aerosols in WRF-Chem are assumed internally mixed, the optical properties and direct radiative forcing of individual aerosol species in the atmosphere is not explicitly calculated. Instead, the methodology described in Zhao et al.[104] is used to diagnose the optical depth and direct radiative effect of individual aerosol species. Therefore, large uncertainties in estimating radiative effects of one individual aerosol species can be introduced in the case of very low mass concentrations. In this study, we found that dust mass concentrations in the first three bins (0.039 – 0.078, 0.078 – 0.156, and 0.156 – 0.312 μm) are quite low. Since such low concentrations produce large relative uncertainties in estimating the particle bin's radiative effects, we omitted those bins in our calculation of DRE using the WRF-Chem simulations.

Following Zhao et al.[103], we used a quasi-global channel configuration (using periodic boundary conditions in the zonal direction) with 360 × 145 grid cells (180° W-180° E, 67.5° S-77.5° N) to perform the simulation at 1° horizontal resolution over the period of 2004-2008. The simulations are configured with 35 vertical layers up to 50 hPa. The meteorological initial and lateral boundary (only for the meridional direction) conditions are derived from the National Center for Environmental Prediction final analysis (NCEP/FNL) data at 1° horizontal resolution and 6 h temporal intervals. The modeled wind components and atmospheric temperature are nudged towards the NCEP/FNL reanalysis data with a nudging timescale of 6 hr[111]. The chemical initial and boundary (only for the meridional direction) conditions are taken from the default profiles in WRF-Chem, which are the same as those used by McKeen et al.[112] and are based on averages of mid-latitude aircraft profiles from several field studies over the eastern Pacific Ocean. This study uses a set of selected schemes for model physics, including the MYJ (Mellor–Yamada–Janjic) planetary boundary layer scheme, Noah land surface scheme, Morrison 2-moment microphysics scheme, Kain-Fritsch cumulus scheme, and RRTMG longwave and shortwave radiation schemes.

Vertical dust emission fluxes are calculated with the Goddard Chemical Aerosol Radiation Transport (GOCART) dust emission scheme[45], and the emitted dust particles are distributed into the MOSAIC aerosol size bins following the theoretical expression of Kok[10].

5.2 Description of GEOS-Chem simulations

We used simulations with GEOS-Chem (version v9-01-03; http://www.geos-chem.org/) for the years 2004 – 2008 to simulate both the dust aerosol lifetime (Fig. 1d) and the size-resolved radiative effect efficiency (Fig. S3). The GEOS-Chem model incorporates a global three-dimensional simulation of coupled oxidant–aerosol chemistry, run at a resolution of 2° ×2.5° latitude and longitude, and 47 vertical levels. The model is driven by assimilated MERRA meteorology from the Goddard Earth Observing System of the NASA Global Modeling and Assimilation Office (GMAO), including assimilated meteorological fields at 1-hourly and 3-hourly temporal resolution. The aerosol types simulated include sulfate–nitrate–ammonium aerosols[113], and carbonaceous aerosols[114-116], mineral dust[46, 117] and sea salt[118]. Dust emission in GEOS-Chem is based upon the DEAD dust scheme[46], making use of the GOCART source function[45]. Mineral dust mass is transported in four different sized bins (0.1–1.0, 1.0–1.8, 1.8–3.0

and 3.0–6.0 μm), the smallest of which is partitioned into four bins (0.10–0.18, 0.18–0.30, 0.30–0.65 and 0.65–1.00 μm) when deriving optical properties, owing to the strong size dependence of extinction for sub-micron aerosol. Dust emission is modified from the standard model to treat 10-m wind fields as a Weibull distribution based on sub-grid wind statistics[119]. Aerosol optical depth (AOD) is calculated online assuming log-normal size distributions of externally mixed aerosols and is a function of the local relative humidity to account for hygroscopic growth[120]. Aerosol optical properties employed here are based on the Global Aerosol Data Set (GADS)[121] with modifications to the size distribution based on field observations[41, 122, 123], and modifications to the dust refractive indices to match the observed lower SW absorption[124]. The refractive indices for each species are interpolated to the 30 wavelengths, between 230 nm and 56 μm, used by the radiative transfer code (RRTMG) coupled with GEOS-Chem[125]. Surface albedo and emissivity are generated from MODIS (MOD11C2 and MCD43C3 products) to provide 8-day averages for a climatology between 2002 and 2007. Cloud optical properties are calculated based on liquid and ice optical depths from the MERRA meteorology with cloud overlap treated using the Monte Carlo independent column approximation (McICA)[126]. The radiative transfer code is run twice every 3 hours in the simulation, once to calculate the flux with all aerosol and a second time with only non-dust aerosol. The difference yields the direct radiative effect (DRE) of dust aerosols.

5.3 Description of HadGEM simulations

The design and the implementation of the UK MetOffice HadGEM2 model family is described in Martin et al.[127] in detail. For our experiment, we simulated the dust aerosol lifetime (Fig. 1d) using the HadGEM2-A model version, which is the atmosphere only version of the global model, run with prescribed SSTs and sea ice climatology updated every 24 hours. Both are based on the Reynolds SST Analysis[128], averaged over the 1995-2005 period. The vertically-extended HI-TOP version of the model was used, with 85 levels extending to 85km height. The horizontal resolution is 1.25 degrees (latitudinal) by 1.875 degrees (longitudinal), which produces a global grid of 192 x 145 grid cells (N96). This is equivalent to a surface resolution of about 208x139 km^2 at the Equator, reducing to 120x139 km^2 at 55 degrees of latitude.

Six aerosol species are incorporated in the model using the CLASSIC aerosol scheme[129]: sulfate, black carbon, biomass burning elemental carbon, fossil fuel organic carbon, mineral dust, and sea salt aerosols. We use monthly averages of Atmospheric Optical Depth (AOD) at 550 nm wavelength for each component, which is available as a prognostic model quantity, except for Sea Salt when it is a diagnosed quantity. Emission datasets for aerosol precursors and primary aerosols have been revised with the HadGEM2 family, using datasets created in support of CMIP5[129-132].

The models dust emission scheme has remained unchanged compared to earlier versions of HadGEM[133, 134]. It is based on the widely used emission parameterization developed by Marticorena and Bergametti [12]. The horizontal flux is calculated for 9 model size bins with boundaries at 0.0316, 0.1, 0.316, 1, 3.16, 10, 31.6, 100, 316 and 1000 μm radius. The vertical emission flux is calculated for 6 model size bins in the size range between 0.0316 to 31.6 μm radius (same bin intervals). The horizontal-to-vertical-mass flux ratio is assumed to be a constant of proportionality as a function of particle size. The mass fraction of particles in each size bin is calculated off-line from the clay, silt and sand fraction data from the International Geosphere-Biosphere Programme (IGBP) global soil data. The threshold friction velocity is also fixed for each size bin. Soil moisture and roughness corrections follow the method of Fecan et al.[135] and Marticorena and Bergametti [12], respectively.

In order to constrain the dust emission flux over major source regions, the concept of preferential sources that vary as a function of topography is applied[45]. Once emitted, the dust aerosols are treated as independent tracers in the atmosphere, such as all the other aerosol species. Sedimentation and turbulent mixing are considered as dry removal mechanisms of dust particles from the atmosphere. Wet removal due to precipitation scavenging within and below cloud for both large-scale and convective precipitation is included using a first-order removal rate[133]. Finally, dust-radiation interaction through SW and LW direct effects is permitted in the model.

References

1. Dufresne, J.L., Gautier, C., Ricchiazzi, P. & Fouquart, Y. Longwave scattering effects of mineral aerosols. *J. Atmos. Sci.* **59**, 1959-1966 (2002).
2. Miller, R.L. *et al.* Mineral dust aerosols in the NASA goddard institute for Space Sciences ModelE atmospheric general circulation model. *Journal of Geophysical Research-Atmospheres* **111**, D06208 (2006).
3. Gillette, D.A., Blifford, I.H. & Fenster, C.R. Measurements of aerosol size distributions and vertical fluxes of aerosols on land subject to wind erosion. *J. Appl. Meteor.* **11**, 977-987 (1972).
4. Gillette, D.A., Blifford, I.H. & Fryrear, D.W. Influence of wind velocity on size distributions of aerosols generated by wind erosion of soils. *Journal of Geophysical Research* **79**, 4068-4075 (1974).
5. Gillette, D.A. On the production of soil wind erosion having the potential for long range transport. *J. Rech. Atmos.* **8**, 734-744 (1974).
6. Fratini, G., Ciccioli, P., Febo, A., Forgione, A. & Valentini, R. Size-segregated fluxes of mineral dust from a desert area of northern China by eddy covariance. *Atmospheric Chemistry and Physics* **7**, 2839-2854 (2007).
7. Sow, M., Alfaro, S.C., Rajot, J.L. & Marticorena, B. Size resolved dust emission fluxes measured in Niger during 3 dust storms of the AMMA experiment. *Atmospheric Chemistry and Physics* **9**, 3881-3891 (2009).
8. Shao, Y., Ishizuka, M., Mikami, M. & Leys, J.F. Parameterization of size-resolved dust emission and validation with measurements. *Journal of Geophysical Research-Atmospheres* **116**, D08203 (2011).
9. Rosenberg, P.D. *et al.* Quantifying particle size and turbulent scale dependence of dust flux in the Sahara using aircraft measurements. *Journal of Geophysical Research-Atmospheres* **119**, 7577-7598 (2014).
10. Kok, J.F. A scaling theory for the size distribution of emitted dust aerosols suggests climate models underestimate the size of the global dust cycle. *Proc. Natl. Acad. Sci. U. S. A.* **108**, 1016-1021 (2011).
11. Kok, J.F. *et al.* An improved dust emission model - Part 1: Model description and comparison against measurements. *Atmospheric Chemistry and Physics* **14**, 13023-13041 (2014).
12. Marticorena, B. & Bergametti, G. Modeling the atmospheric dust cycle .1. Design of a soil-derived emission scheme. *Journal of Geophysical Research-Atmospheres* **100**, 16415-16430 (1995).
13. Shao, Y.P. Simplification of a dust emission scheme and comparison with data. *Journal of Geophysical Research-Atmospheres* **109** (2004).
14. Kok, J.F. Does the size distribution of mineral dust aerosols depend on the wind speed at emission? *Atmospheric Chemistry and Physics* **11**, 10149-10156 (2011).
15. Mahowald, N. *et al.* The size distribution of desert dust aerosols and its impact on the Earth system. *Aeolian Research* **15**, 53-71 (2014).
16. Reid, J.S. *et al.* Dynamics of southwest Asian dust particle size characteristics with implications for global dust research. *Journal of Geophysical Research-Atmospheres* **113** (2008).
17. Denjean, C. *et al.* Size distribution and optical properties of African mineral dust after intercontinental transport. *Journal of Geophysical Research-Atmospheres* **121**, 7117-7138 (2016).
18. Hinds, W.C. *Aerosol technology: Properties, Behavior, and measurement of airborne particles*, Edn. 2. (John Wiley & Sons, New York; 1999).
19. Reid, J.S. *et al.* Comparison of size and morphological measurements of coarse mode dust particles from Africa. *Journal of Geophysical Research-Atmospheres* **108** (2003).
20. Kaaden, N. *et al.* State of mixing, shape factor, number size distribution, and hygroscopic growth of the Saharan anthropogenic and mineral dust aerosol at Tinfou, Morocco. *Tellus Ser. B-Chem. Phys. Meteorol.* **61**, 51-63 (2009).

21. Cartwright, J. Particle shape factors. *Ann. Occup. Hyg.* **5**, 163-171 (1962).
22. Davies, C.N. Particle-fluid interaction. *Journal of Aerosol Science* **10**, 477-& (1979).
23. Bevington, P.R. & Robinson, D.K. *Data reduction and error analysis.* (McGraw-Hill, New York; 2003).
24. Ishizuka, M. *et al.* Power law relation between size-resolved vertical dust flux and friction velocity measured in a fallow wheat field. *Aeolian Research* **12**, 87-99 (2014).
25. Ishizuka, M. *et al.* Effects of soil moisture and dried raindroplet crust on saltation and dust emission. *Journal of Geophysical Research-Atmospheres* **113** (2008).
26. Weinzierl, B. *et al.* Airborne measurements of dust layer properties, particle size distribution and mixing state of Saharan dust during SAMUM 2006. *Tellus Ser. B-Chem. Phys. Meteorol.* **61**, 96-117 (2009).
27. Kandler, K. *et al.* Size distribution, mass concentration, chemical and mineralogical composition and derived optical parameters of the boundary layer aerosol at Tinfou, Morocco, during SAMUM 2006. *Tellus Ser. B-Chem. Phys. Meteorol.* **61**, 32-50 (2009).
28. Schladitz, A. *et al.* In situ measurements of optical properties at Tinfou (Morocco) during the Saharan Mineral Dust Experiment SAMUM 2006. *Tellus Ser. B-Chem. Phys. Meteorol.* **61**, 64-78 (2009).
29. Nousiainen, T. & Kandler, K. Light scattering by atmospheric mineral dust particles, in *Light Scattering Reviews*, Vol. 9. (ed. A. kokhanovsky) (Springer - Verlag, Berlin Heidelberg; 2015).
30. Efron, B. *The jackknife, the bootstrap, and other resampling plans*. (Capital City Press, Montpelier, Vermont; 1982).
31. Chernick, M.R. *Bootstrap methods : a guide for practitioners and researchers*. (Wiley-Interscience, Hoboken, N.J.; 2007).
32. Perlwitz, J.P., Garcia-Pando, C.P. & Miller, R.L. Predicting the mineral composition of dust aerosols - Part 1: Representing key processes. *Atmospheric Chemistry and Physics* **15**, 11593-11627 (2015).
33. Yue, X., Wang, H., Wang, Z. & Fan, K. Simulation of dust aerosol radiative feedback using the Global Transport Model of Dust: 1. Dust cycle and validation. *Journal of Geophysical Research-Atmospheres* **114** (2009).
34. Kok, J.F., Albani, S., Mahowald, N.M. & Ward, D.S. An improved dust emission model - Part 2: Evaluation in the Community Earth System Model, with implications for the use of dust source functions. *Atmospheric Chemistry and Physics* **14**, 13043-13061 (2014).
35. Liu, J., Mauzerall, D.L., Horowitz, L.W., Ginoux, P. & Fiore, A.M. Evaluating inter-continental transport of fine aerosols: (1) Methodology, global aerosol distribution and optical depth. *Atmos. Environ.* **43**, 4327-4338 (2009).
36. Liu, X. *et al.* Uncertainties in global aerosol simulations: Assessment using three meteorological data sets. *Journal of Geophysical Research-Atmospheres* **112** (2007).
37. Colarco, P.R., Kahn, R.A., Remer, L.A. & Levy, R.C. Impact of satellite viewing-swath width on global and regional aerosol optical thickness statistics and trends. *Atmospheric Measurement Techniques* **7**, 2313-2335 (2014).
38. Buchard, V. *et al.* Using the OMI aerosol index and absorption aerosol optical depth to evaluate the NASA MERRA Aerosol Reanalysis. *Atmospheric Chemistry and Physics* **15**, 5743-5760 (2015).
39. Zhang, J. & Reid, J.S. A decadal regional and global trend analysis of the aerosol optical depth using a data-assimilation grade over-water MODIS and Level 2 MISR aerosol products. *Atmospheric Chemistry and Physics* **10**, 10949-10963 (2010).
40. Buchard, V. *et al.* Evaluation of the surface PM2.5 in Version 1 of the NASA MERRA Aerosol Reanalysis over the United States. *Atmos. Environ.* **125**, 100-111 (2016).
41. Ridley, D.A., Heald, C.L. & Ford, B. North African dust export and deposition: A satellite and model perspective. *Journal of Geophysical Research-Atmospheres* **117** (2012).

42. Wilks, D.S. *Statistical Methods in the Amtospheric Sciences*, Edn. 3rd. (Academic Press, Oxford, UK; 2011).
43. Kinne, S. *et al.* An AeroCom initial assessment - optical properties in aerosol component modules of global models. *Atmospheric Chemistry and Physics* **6**, 1815-1834 (2006).
44. Mahowald, N.M. *et al.* Change in atmospheric mineral aerosols in response to climate: Last glacial period, preindustrial, modern, and doubled carbon dioxide climates. *J. Geophys. Res.* **111**, D10202 (2006).
45. Ginoux, P. *et al.* Sources and distributions of dust aerosols simulated with the GOCART model. *J. Geophys. Res.-Atmos.* **106**, 20255-20273 (2001).
46. Zender, C.S., Bian, H. & Newman, D. The mineral Dust Entrainment And Deposition (DEAD) model: Description and 1990s dust climatology. *Journal of Geophysical Research* **108**, 4416 (2003).
47. Reddy, M.S. *et al.* Estimates of global multicomponent aerosol optical depth and direct radiative perturbation in the Laboratoire de Meteorologie Dynamique general circulation model. *Journal of Geophysical Research-Atmospheres* **110** (2005).
48. Takemura, T., Uno, I., Nakajima, T., Higurashi, A. & Sano, I. Modeling study of long-range transport of Asian dust and anthropogenic aerosols from East Asia. *Geophysical Research Letters* **29** (2002).
49. Takemura, T., Nozawa, T., Emori, S., Nakajima, T.Y. & Nakajima, T. Simulation of climate response to aerosol direct and indirect effects with aerosol transport-radiation model. *Journal of Geophysical Research-Atmospheres* **110** (2005).
50. Takemura, T. *et al.* A simulation of the global distribution and radiative forcing of soil dust aerosols at the Last Glacial Maximum. *Atmospheric Chemistry and Physics* **9**, 3061-3073 (2009).
51. Morcrette, J.J. *et al.* Aerosol analysis and forecast in the European Centre for Medium-Range Weather Forecasts Integrated Forecast System: Forward modeling. *Journal of Geophysical Research-Atmospheres* **114** (2009).
52. Berglen, T.F., Berntsen, T.K., Isaksen, I.S.A. & Sundet, J.K. A global model of the coupled sulfur/oxidant chemistry in the troposphere: The sulfur cycle. *Journal of Geophysical Research-Atmospheres* **109** (2004).
53. Myhre, G. *et al.* Comparison of the radiative properties and direct radiative effect of aerosols from a global aerosol model and remote sensing data over ocean. *Tellus Series B-Chemical and Physical Meteorology* **59**, 115-129 (2007).
54. Balkanski, Y., Schulz, M., Moulin, C. & Ginoux, P. The formulation of dust emissions on global scale: formulation and validation using satellite retrievals, in *Emissions of Atmospheric Trace Compounds*. (eds. C. Granier, P. Artaxo & C. Reeves) 239-267 (Kluwer Academic Publishers, Dordrecht; 2004).
55. Stier, P. *et al.* The aerosol-climate model ECHAM5-HAM. *Atmospheric Chemistry and Physics* **5**, 1125-1156 (2005).
56. Ghan, S.J. & Easter, R.C. Impact of cloud-borne aerosol representation on aerosol direct and indirect effects. *Atmospheric Chemistry and Physics* **6**, 4163-4174 (2006).
57. Krol, M. *et al.* The two-way nested global chemistry-transport zoom model TM5: algorithm and applications. *Atmospheric Chemistry and Physics* **5**, 417-432 (2005).
58. de Meij, A. *et al.* The sensitivity of aerosol in Europe to two different emission inventories and temporal distribution of emissions. *Atmospheric Chemistry and Physics* **6**, 4287-4309 (2006).
59. Ridley, D.A., Heald, C.L., Kok, J.F. & Zhao, C. An observationally-constrained estimate of global dust aerosol optical depth. *Atmospheric Chemistry and Physics* **16**, 15097-15117 (2016).
60. Meng, Z.K. *et al.* Single-scattering properties of tri-axial ellipsoidal mineral dust aerosols: A database for application to radiative transfer calculations. *Journal of Aerosol Science* **41**, 501-512 (2010).

61. Patterson, E.M., Gillette, D.A. & Stockton, B.H. Complex index of refraction between 300 and 700 nm for saharan aerosols. *Journal of Geophysical Research-Oceans and Atmospheres* **82**, 3153-3160 (1977).
62. Dubovik, O. *et al.* Variability of absorption and optical properties of key aerosol types observed in worldwide locations. *J. Atmos. Sci.* **59**, 590-608 (2002).
63. Kim, D. *et al.* Dust optical properties over North Africa and Arabian Peninsula derived from the AERONET dataset. *Atmospheric Chemistry and Physics* **11**, 10733-10741 (2011).
64. Muller, D. *et al.* Comparison of optical and microphysical properties of pure Saharan mineral dust observed with AERONET Sun photometer, Raman lidar, and in situ instruments during SAMUM 2006. *Journal of Geophysical Research-Atmospheres* **117**, 25 (2012).
65. Deluisi, J.J. *et al.* Results of a comprehensive atmospheric aerosol radiation experiment in southwestern united-states .2. Radiation flux measurements and theoretical interpretation. *Journal of Applied Meteorology* **15**, 455-463 (1976).
66. Grams, G.W., Blifford, I.H., Gillette, D.A. & Russell, P.B. Complex index of refraction of airborn soil particles. *Journal of Applied Meteorology* **13**, 459-471 (1974).
67. Redmond, H.E., Dial, K.D. & Thompson, J.E. Light scattering and absorption by wind blown dust: Theory, measurement, and recent data. *Aeolian Research* **2**, 5-26 (2010).
68. Seinfeld, J.H. *et al.* ACE-ASIA - Regional climatic and atmospheric chemical effects of Asian dust and pollution. *Bulletin of the American Meteorological Society* **85**, 367-+ (2004).
69. Denjean, C. *et al.* Size distribution and optical properties of mineral dust aerosols transported in the western Mediterranean. *Atmospheric Chemistry and Physics* **16**, 1081-1104 (2016).
70. Denjean, C. *et al.* Long-range transport across the Atlantic in summertime does not enhance the hygroscopicity of African mineral dust. *Geophys. Res. Lett.* **42**, 7835-7843 (2015).
71. Sokolik, I., Andronova, A. & Johnson, T.C. Complex refractive-index of atmospheric dust aerosols. *Atmospheric Environment Part a-General Topics* **27**, 2495-2502 (1993).
72. Kandler, K. *et al.* Chemical composition and complex refractive index of Saharan Mineral Dust at Izana, Tenerife (Spain) derived by electron microscopy. *Atmos. Environ.* **41**, 8058-8074 (2007).
73. Clarke, A.D. *et al.* Size distributions and mixtures of dust and black carbon aerosol in Asian outflow: Physiochemistry and optical properties. *Journal of Geophysical Research-Atmospheres* **109** (2004).
74. Balkanski, Y., Schulz, M., Claquin, T. & Guibert, S. Reevaluation of Mineral aerosol radiative forcings suggests a better agreement with satellite and AERONET data. *Atmospheric Chemistry and Physics* **7**, 81-95 (2007).
75. Lafon, S., Sokolik, I.N., Rajot, J.L., Caquineau, S. & Gaudichet, A. Characterization of iron oxides in mineral dust aerosols: Implications for light absorption. *Journal of Geophysical Research-Atmospheres* **111** (2006).
76. Sokolik, I.N. & Toon, O.B. Incorporation of mineralogical composition into models of the radiative properties of mineral aerosol from UV to IR wavelengths. *Journal of Geophysical Research-Atmospheres* **104**, 9423-9444 (1999).
77. Reid, E.A. *et al.* Characterization of African dust transported to Puerto Rico by individual particle and size segregated bulk analysis. *Journal of Geophysical Research-Atmospheres* **108** (2003).
78. Okada, K., Heintzenberg, J., Kai, K.J. & Qin, Y. Shape of atmospheric mineral particles collected in three Chinese arid-regions. *Geophysical Research Letters* **28**, 3123-3126 (2001).
79. Chou, C. *et al.* Size distribution, shape, and composition of mineral dust aerosols collected during the African Monsoon Multidisciplinary Analysis Special Observation Period 0: Dust and Biomass-Burning Experiment field campaign in Niger, January 2006. *Journal of Geophysical Research-Atmospheres* **113**, D00c10 (2008).
80. Kandler, K. *et al.* Electron microscopy of particles collected at Praia, Cape Verde, during the Saharan Mineral Dust Experiment: particle chemistry, shape, mixing state and complex refractive index. *Tellus Ser. B-Chem. Phys. Meteorol.* **63**, 475-496 (2011).

81. Scheuvens, D. & Kandler, K. On composition, morphology, and size distribution of airborne mineral dust, in *Mineral dust: A key player in the Earth system*. (eds. P. Knippertz & J.B.W. Stuut) 15-49 (Springer, Dordrecht; 2014).
82. Coz, E. *et al.* Individual particle characteristics of North African dust under different long-range transport scenarios. *Atmos. Environ.* **43**, 1850-1863 (2009).
83. Scheuvens, D. *et al.* Individual-particle analysis of airborne dust samples collected over Morocco in 2006 during SAMUM 1. *Tellus Ser. B-Chem. Phys. Meteorol.* **63**, 512-530 (2011).
84. Veghte, D.P. & Freedman, M.A. Facile Method for Determining the Aspect Ratios of Mineral Dust Aerosol by Electron Microscopy. *Aerosol Science and Technology* **48**, 715-724 (2014).
85. Kalashnikova, O.V. & Sokolik, I.N. Modeling the radiative properties of nonspherical soil-derived mineral aerosols. *Journal of Quantitative Spectroscopy & Radiative Transfer* **87**, 137-166 (2004).
86. Vilaplana, R., Luna, R. & Guirado, D. The shape influence on the overall single scattering properties of a sample in random orientation. *Journal of Quantitative Spectroscopy & Radiative Transfer* **112**, 1838-1847 (2011).
87. Zakharova, N.T. & Mishchenko, M.I. Scattering properties of needlelike and platelike ice spheroids with moderate size parameters. *Applied Optics* **39**, 5052-5057 (2000).
88. Sun, B., Yang, P. & Kattawar, G.W. Many-body iterative T-matrix method for large aspect ratio particles. *Journal of Quantitative Spectroscopy & Radiative Transfer* **127**, 165-175 (2013).
89. Mätzler, C. (Institut für Angewandte Physik, Bern, Switzerland; 2002).
90. Colarco, P.R. *et al.* Impact of radiatively interactive dust aerosols in the NASA GEOS-5 climate model: Sensitivity to dust particle shape and refractive index. *Journal of Geophysical Research-Atmospheres* **119**, 753-786 (2014).
91. Stevens, B. Rethinking the Lower Bound on Aerosol Radiative Forcing. *J. Climate* **28**, 4794-4819 (2015).
92. Albani, S. *et al.* Improved dust representation in the Community Atmosphere Model. *J. Adv. Model. Earth Syst.* **6**, 541-570 (2014).
93. Conley, A.J., Lamarque, J.F., Vitt, F., Collins, W.D. & Kiehl, J. PORT, a CESM tool for the diagnosis of radiative forcing. *Geoscientific Model Development* **6**, 469-476 (2013).
94. Sinyuk, A., Torres, O. & Dubovik, O. Combined use of satellite and surface observations to infer the imaginary part of refractive index of Saharan dust. *Geophysical Research Letters* **30** (2003).
95. Forster, P. *et al.* Changes in Atmospheric Constituents and in Radiative Forcing., in *Climate Change 2007: The Physical Science Basis.* (ed. S. Solomon, D. Qin, M. Manning, Z. Chen, M. Marquis, K.B. Averyt, M.Tignor and H.L. Miller) (Cambridge University Press, Cambridge, United Kingdom and New York, NY, USA; 2007).
96. Tegen, I. & Lacis, A.A. Modeling of particle size distribution and its influence on the radiative properties of mineral dust aerosol. *Journal of Geophysical Research-Atmospheres* **101**, 19237-19244 (1996).
97. Hansen, J.E. & Travis, L.D. Light-scattering in planetary atmospheres. *Space Sci. Rev.* **16**, 527-610 (1974).
98. Huneeus, N. *et al.* Global dust model intercomparison in AeroCom phase I. *Atmospheric Chemistry and Physics* **11**, 7781-7816 (2011).
99. Mahowald, N.M. *et al.* Climate response and radiative forcing from mineral aerosols during the last glacial maximum, pre-industrial, current and doubled-carbon dioxide climates. *Geophysical Research Letters* **33**, L20705 (2006).
100. Zaveri, R.A., Easter, R.C., Fast, J.D. & Peters, L.K. Model for Simulating Aerosol Interactions and Chemistry (MOSAIC). *Journal of Geophysical Research-Atmospheres* **113** (2008).
101. Zaveri, R.A. & Peters, L.K. A new lumped structure photochemical mechanism for large-scale applications. *Journal of Geophysical Research-Atmospheres* **104**, 30387-30415 (1999).

102. Fast, J.D. *et al.* Evolution of ozone, particulates, and aerosol direct radiative forcing in the vicinity of Houston using a fully coupled meteorology-chemistry-aerosol model. *Journal of Geophysical Research-Atmospheres* **111** (2006).
103. Zhao, C. *et al.* Uncertainty in modeling dust mass balance and radiative forcing from size parameterization. *Atmospheric Chemistry and Physics* **13**, 10733-10753 (2013).
104. Zhao, C., Leung, L.R., Easter, R., Hand, J. & Avise, J. Characterization of speciated aerosol direct radiative forcing over California. *Journal of Geophysical Research-Atmospheres* **118**, 2372-2388 (2013).
105. Hess, M., Koepke, P. & Schult, I. Optical properties of aerosols and clouds: The software package OPAC. *Bulletin of the American Meteorological Society* **79**, 831-844 (1998).
106. Zhao, C. *et al.* The spatial distribution of mineral dust and its shortwave radiative forcing over North Africa: modeling sensitivities to dust emissions and aerosol size treatments. *Atmospheric Chemistry and Physics* **10**, 8821-8838 (2010).
107. Zhao, C., Liu, X., Leung, L.R. & Hagos, S. Radiative impact of mineral dust on monsoon precipitation variability over West Africa. *Atmospheric Chemistry and Physics* **11**, 1879-1893 (2011).
108. Barnard, J.C., Fast, J.D., Paredes-Miranda, G., Arnott, W.P. & Laskin, A. Technical Note: Evaluation of the WRF-Chem "Aerosol Chemical to Aerosol Optical Properties" Module using data from the MILAGRO campaign. *Atmospheric Chemistry and Physics* **10**, 7325-7340 (2010).
109. Mlawer, E.J., Taubman, S.J., Brown, P.D., Iacono, M.J. & Clough, S.A. Radiative transfer for inhomogeneous atmospheres: RRTM, a validated correlated-k model for the longwave. *Journal of Geophysical Research-Atmospheres* **102**, 16663-16682 (1997).
110. Iacono, M.J., Mlawer, E.J., Clough, S.A. & Morcrette, J.J. Impact of an improved longwave radiation model, RRTM, on the energy budget and thermodynamic properties of the NCAR community climate model, CCM3. *Journal of Geophysical Research-Atmospheres* **105**, 14873-14890 (2000).
111. Stauffer, D.R. & Seaman, N.L. Use of 4-dimensional data assimilation in a limited-area mesoscale model .1. Experiments with synoptic-scale data. *Monthly Weather Review* **118**, 1250-1277 (1990).
112. McKeen, S.A. *et al.* Ozone production from Canadian wildfires during June and July of 1995. *Journal of Geophysical Research-Atmospheres* **107** (2002).
113. Park, R.J., Jacob, D.J., Field, B.D., Yantosca, R.M. & Chin, M. Natural and transboundary pollution influences on sulfate-nitrate-ammonium aerosols in the United States: Implications for policy. *Journal of Geophysical Research-Atmospheres* **109** (2004).
114. Park, R.J., Jacob, D.J., Chin, M. & Martin, R.V. Sources of carbonaceous aerosols over the United States and implications for natural visibility. *Journal of Geophysical Research-Atmospheres* **108** (2003).
115. Liao, H., Henze, D.K., Seinfeld, J.H., Wu, S. & Mickley, L.J. Biogenic secondary organic aerosol over the United States: Comparison of climatological simulations with observations. *Journal of Geophysical Research-Atmospheres* **112** (2007).
116. Henze, D.K. *et al.* Global modeling of secondary organic aerosol formation from aromatic hydrocarbons: high- vs. low-yield pathways. *Atmospheric Chemistry and Physics* **8**, 2405-2420 (2008).
117. Fairlie, T.D., Jacob, D.J. & Park, R.J. The impact of transpacific transport of mineral dust in the United States. *Atmos. Environ.* **41**, 1251-1266 (2007).
118. Alexander, B. *et al.* Sulfate formation in sea-salt aerosols: Constraints from oxygen isotopes. *Journal of Geophysical Research-Atmospheres* **110** (2005).
119. Ridley, D.A., Heald, C.L., Pierce, J.R. & Evans, M.J. Toward resolution-independent dust emissions in global models: Impacts on the seasonal and spatial distribution of dust. *Geophysical Research Letters* **40**, 2873-2877 (2013).

120. Martin, R.V., Jacob, D.J., Yantosca, R.M., Chin, M. & Ginoux, P. Global and regional decreases in tropospheric oxidants from photochemical effects of aerosols. *Journal of Geophysical Research-Atmospheres* **108** (2003).
121. Koepke, P., Hess, M., Schult, I. & Shettle, E., Vol. Report 243 (Max Planck Institute for Meteorology, Hamburg, 1997).
122. Jaegle, L., Quinn, P.K., Bates, T.S., Alexander, B. & Lin, J.T. Global distribution of sea salt aerosols: new constraints from in situ and remote sensing observations. *Atmospheric Chemistry and Physics* **11**, 3137-3157 (2011).
123. Drury, E. *et al.* Synthesis of satellite (MODIS), aircraft (ICARTT), and surface (IMPROVE, EPA-AQS, AERONET) aerosol observations over eastern North America to improve MODIS aerosol retrievals and constrain surface aerosol concentrations and sources. *Journal of Geophysical Research-Atmospheres* **115** (2010).
124. Sinyuk, A., Torres, O. & Dubovik, O. Combined use of satellite and surface observations to infer the imaginary part of refractive index of Saharan dust. *Geophys. Res. Lett.* **30**, 1081 (2003).
125. Heald, C.L. *et al.* Contrasting the direct radiative effect and direct radiative forcing of aerosols. *Atmospheric Chemistry and Physics* **14**, 5513-5527 (2014).
126. Pincus, R., Barker, H.W. & Morcrette, J.J. A fast, flexible, approximate technique for computing radiative transfer in inhomogeneous cloud fields. *Journal of Geophysical Research-Atmospheres* **108**, 4376 (2003).
127. Martin, G.M. *et al.* The HadGEM2 family of Met Office Unified Model climate configurations. *Geoscientific Model Development* **4**, 723-757 (2011).
128. Reynolds, J.F. *et al.* Global desertification: Building a science for dryland development. *Science* **316**, 847-851 (2007).
129. Bellouin, N. *et al.* in Hadley Centre Technical Note, Vol. 73 (Met Office Hadley Centre, 2007).
130. Jones, A., Roberts, D.L., Woodage, M.J. & Johnson, C.E. Indirect sulphate aerosol forcing in a climate model with an interactive sulphur cycle. *Journal of Geophysical Research-Atmospheres* **106**, 20293-20310 (2001).
131. Roberts, D.L. & Jones, A. Climate sensitivity to black carbon aerosol from fossil fuel combustion. *Journal of Geophysical Research-Atmospheres* **109** (2004).
132. Dentener, F. *et al.* Emissions of primary aerosol and precursor gases in the years 2000 and 1750 prescribed data-sets for AeroCom. *Atmospheric Chemistry and Physics* **6**, 4321-4344 (2006).
133. Woodward, S. Modeling the atmospheric life cycle and radiative impact of mineral dust in the Hadley Centre climate model. *Journal of Geophysical Research-Atmospheres* **106**, 18155-18166 (2001).
134. Woodward, S. in Hadley Centre Technical Note 87 (Met Office Hadley Centre; 2011).
135. Fécan, F., Marticorena, B. & Bergametti, G. Parametrization of the increase of the aeolian erosion threshold wind friction velocity due to soil moisture for arid and semi-arid areas. *Ann Geophys-Atm Hydr* **17**, 149-157 (1999).